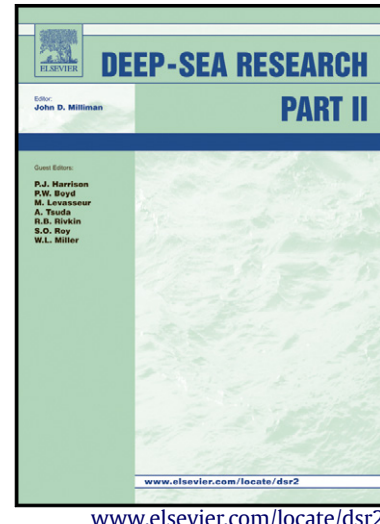


# Author's Accepted Manuscript



Small-scale deformation of an Arctic sea ice  
floe detected by GPS and satellite imagery

Byongjun Hwang, Pedro Elosegui, Jeremy Wilk-  
inson

PII: S0967-0645(15)00018-1  
DOI: <http://dx.doi.org/10.1016/j.dsr2.2015.01.007>  
Reference: DSRII3791

To appear in: *Deep-Sea Research II*

Cite this article as: Byongjun Hwang, Pedro Elosegui, Jeremy Wilkinson, Small-scale deformation of an Arctic sea ice floe detected by GPS and satellite imagery, *Deep-Sea Research II*, <http://dx.doi.org/10.1016/j.dsr2.2015.01.007>

This is a PDF file of an unedited manuscript that has been accepted for publication. As a service to our customers we are providing this early version of the manuscript. The manuscript will undergo copyediting, typesetting, and review of the resulting galley proof before it is published in its final citable form. Please note that during the production process errors may be discovered which could affect the content, and all legal disclaimers that apply to the journal pertain.

# Small-scale deformation of an Arctic sea ice floe detected by GPS and satellite imagery

Byongjun Hwang<sup>1\*</sup>, Pedro Elosegui<sup>2,3</sup>, and Jeremy Wilkinson<sup>4</sup>

<sup>1</sup> Scottish Association for Marine Science, Oban, Argyll, PA37 1QA, UK

<sup>2</sup> Institute of Marine Sciences (ICM-CSIC), Barcelona, Spain

<sup>3</sup> Massachusetts Institute of Technology, Haystack Observatory, Westford, MA, USA

<sup>4</sup> British Antarctic Survey, High Cross, Madingley Road, Cambridge, CB3 0ET, UK

\* Corresponding author

Tel: +44-1631-559-428; Fax: +44-1631-559-001

E-mail addresses: phil.hwang@sams.ac.uk

## Abstract

Small-scale ( $\sim$ 100 to 200 m) deformations of an Arctic sea ice floe were detected from multiple GPS-equipped buoys that were deployed on the same ice floe. Over a nine-month period three deformation events were recorded. At each case the event was of limited duration, each lasting less than a day. The events were highly compressive in nature with the area occupied by the buoy array decreasing by over half of the original area. The strain rate during the deformation, of the order of  $10^{-5}$  s $^{-1}$ , is about three orders of magnitude larger than previous estimates for brittle fracturing for cracks of about 100 m in length. On the 2-day time scale, the strain rate became too small and none of the deformation events could be detected. This suggests that satellite data with longer time scales may significantly underestimate the amount of intermittent, small-scale brittle failure of total deformation. Taken as a whole, our results show the influence that large-scale wind stress can have on small-scale deformation. However, it is important to note that the impact of large-scale wind stress is also dependent on the properties of sea ice as well as on the spatial and temporal evolution of the underlying forces that influence the fracturing process.

## 1. Introduction

Arctic sea ice is in a constant state of deformation (e.g., Kwok and Sulsky, 2010). Under the action of external forces (primarily winds and ocean currents), a continuous sheet of sea ice can be deformed to form a number of ice features such as leads, ridges, and rubble fields. Interestingly, a number of authors have shown that the rate of deformation of Arctic sea ice has increased in response to the recent decrease in sea ice extent and thickness (e.g., Rampal et al., 2009; Zhang et al., 2012), particularly so after the record minimum of ice extent in 2007 (Kwok and Cunningham, 2012).

Previous studies using satellite and drifting buoy data indicate that sea ice deformation is highly heterogeneous, localized, intermittent, and displays multifractal, scale-invariant behaviour (e.g., Marsan et al. 2004; Rampal et al., 2008). Ice deformation is not only dependent on external forcing but is also a function of sea ice compactness, strength, and heterogeneity. Compactness is a measure of ice

concentration. In winter, ice concentration in the Arctic Ocean is close to 100%, while in spring and summer ice concentration can decrease significantly. Ice strength is a difficult variable to monitor but it can be estimated from the ice temperature profile (brine volume) and ice type (Kovacs, 1996). The brine volume, which is a function of temperature and salinity, increases with temperature. For example, warm ice has a high volume of liquid brine and is thus weaker than cold ice. Heterogeneity relates to the horizontal distribution of ice types, cracks, leads and refrozen melt ponds. As these properties vary spatially and temporally this, important parameter is difficult to estimate.

For the brittle failure of sea ice, Marsan et al. (2004) obtained a strain rate of  $10^{-4} \text{ s}^{-1}$  and estimated, at the 3-day time scale, that brittle failure would occur at relatively small percentage of total deformation (about 0.2% of total area). Schulson (2004), on the other hand, estimated that the transition from ductile deformation to brittle failure occurs at a strain rate of  $10^{-8} \text{ s}^{-1}$ . Such low transitional strain rates can be attributed to a relatively high resistance to creep (Schulson, 2004). This wide range of ductile-to-brittle transitional strain rates (ranging from  $10^{-8} \text{ s}^{-1}$  to  $10^{-4} \text{ s}^{-1}$ ) may be due to different length scales for the stress concentrators (i.e., cracks and leads).

Using a combined approach involving satellite imagery and laboratory experiments, Schulson (2004) showed that brittle failure could occur under “moderate” biaxial compression. Such compression produced fracture features in well-organized patterns (spanning from millimetre to hundreds of kilometres), as opposed to random patterns associated with thermal cracks. These types of fractures are called “brittle” compressive shear faults and generally occur when new ice that is located between thicker ice floes grows rigid enough to create a mechanical continuum (Richter-Menge and Elder, 1998).

Hutchings et al. (2011), using an array of GPS drifters spanning distances between 10-140 km, also found sea ice deformation to follow a multi-fractal behaviour (Rampal et al. 2008). When they examined the spectral properties of deformation (which represents the full scaling behaviour, as opposed to Marsan et al. (2004), who considered the scaling properties of sea ice deformation), they found no apparent universal scaling law for ice deformation that could be applied between 10-70 km. This implies that the largest energy dissipation occurs at small spatial scales (e.g., say km scale, or less), as well as decoupling from large-scale

atmospheric wind forcing. This view is supported by Herman and Glowacki (2012), Geiger et al. (2000), Walter and Overland (1993), and others. However, the scaling of deformation at smaller spatial scales remains unresolved, largely for lack of measurements of transient and higher-stress episodes (e.g., Richter-Menge and Elder, 1998; Richter-Menge et al., 2002).

We present observations of several discrete deformation events as captured by a tight network of GPS-equipped drifters deployed on a single ice floe. The network spanned less than 200 m. Over the 9-month duration of this study, a total of three major deformation events occurred. They were clustered over a 10-day period, but each event lasted a day or less. Consequently, the structure of this paper is organized to address two major questions:

- (1) What is the character of Arctic sea ice deformation at sub-km scales?
- (2) How does small-scale deformation connect to large-scale atmospheric forcing?

To address these questions, we present the field observation program in section 2, describe the data and data analysis in section 3, chronicle the three deformation events in section 4, and discuss the results in section 5.

## **2. Background and fieldwork**

### **2.1. Environment and region**

On 13 September 2012, sea ice extent in the Arctic Ocean reached its lowest point since routine satellite observations started in 1978,  $3.4 \times 10^6 \text{ km}^2$ , a drop of about a million square kilometers from the previous minimum, in 2007 (Parkinson and Comiso, 2013). This dramatic loss of sea ice was most evident in the Chukchi Sea and Beaufort Sea, where by mid-August the sea ice edge had retreated beyond  $80^\circ\text{N}$  (Parkinson and Comiso, 2013; also our field observations). The causes of summer sea ice retreat are complex and have been attributed to multiple factors, including overall thinning of the ice and loss of thick multi-year ice (MYI) (Kwok and Rothrock, 2009), a significant storm in early August in the region (Simmonds and Rudeva, 2012), and mechanical breakup and melting of sea ice due to enhanced mixing in the upper ocean (Zhang et al., 2013).

Our team joined the International Arctic Ocean Research Expedition 2012 led by the Korea Polar Research Institute (KOPRI) onboard the icebreaker research

vessel (IBRV) *Araon*. The expedition originally planned to cover the region between the northern Chukchi Sea and the border of East Siberian Sea. However, substantial ice loss in the region prompted the cruise to divert northward in search of suitable ice of adequate sea ice concentration (SIC) for buoy deployment operations. Guided by passive-microwave SIC maps and helicopter reconnaissance surveys, a deployment region was selected in the region bordering the East Siberian Sea and the northern Chukchi Sea ( $81^{\circ} 40.38'N$  and  $174^{\circ} 15.56'E$ ; Figure 1a). The SIC at the time of deployment was more than 70% and comprised a melange of ice floes of various sizes, from tens of meters to tens of kilometres (Figure 1). Larger ice floes mostly consisted of first-year ice (FYI) pans embedded with smaller pieces of MYI that could be recognized by its higher freeboard, undulating topography, and the presence of blue-like melt ponds on their surface.

## 2.2. Ice floe description

The ice floe for the buoy deployment was located about 10 km into the pack from the broken ice edge (Figure 1b). The selected square-shaped floe had sides of approximately 2 km (Figure 1c). It comprised of different ice types frozen together, and contained a high percentage of melt ponds. *Araon* broke a path towards the centre of the floe, and eventually moored in a region of level FYI for the duration of the deployment (Figure 1d). After deployment *Araon* left via the same route as she entered. The track of the ship can be seen as a faint line running from the ship to the bottom right-hand side of Figure 1c.

The area adjacent to the moored ship (about 100 m in radius, green circle in Figure 1c) was level ice and contained very few melt ponds. Ice thickness in this region was about 1 m. Bulk ice salinity measured from an ice core (1.1-m thick) taken nearby the ship was  $1.7 \pm 1.0$  psu, ranging from about 0.2 psu in the top 0.3 m to about 2.8 psu in the bottom 0.4 m. Ice temperature was isothermal at around 0 °C. These conditions resemble typical salinity profile of FYI after melt-water flushing during summer melt (Petrich and Eicken, 2010). The temperature and salinity as well as the smoothness, thickness, and levelness of this part of the ice suggest that the floe was FYI, formed during the previous winter. Surrounding the FYI lay several pieces of MYI with blue-looking melt ponds (i.e., closed, melt ponds not connected to the underlying ocean). At the interface between the MYI and the FYI a chain of melt ponds and small ridging existed (Figure 1d and field observation).

### 2.3. Deployment of buoys

Three types of buoys were deployed on this floe. A short description of each system can be found below, and a summary of the deployment and sampling configurations can be found in Table 1.

(1) The SATICE system is an ice buoy equipped with a geodetic-quality GPS receiving system operated continuously and providing cm-level position estimates. A SATICE buoy also includes a variety of complementary geophysical sensor providing a range of atmospheric, cryospheric, and oceanographic observations (Elosegui et al., 2012). Within this paper we refer to these buoys using the prefix SI. The model numbers deployed were SI03 and SI04.

(2) Sea ice mass balance (IMB) buoys were equipped with a string of thermistors, and a standard-precision (few meters; see below) GPS receiver. They had either (a) a 5-m long chain with 240 thermistor sensors at 2-cm interval or (b) a 10-m long chain with the upper 5 m with 2-cm interval (240 sensors) and the bottom 5 m with 50-cm intervals between sensors (10 sensors). Detailed description of these IMBs is available elsewhere (Jackson et al. 2013). Within this paper we refer to these buoys using the prefix KP. The model numbers deployed were KP01 through KP08.

(3) Seasonal ice mass balance buoy (SIMB) is a floatable IMB that is designed to survive through the summer melt season. They have air temperature and barometric pressure sensors, under ice sounder (distance to the ice bottom), snow sounder (distance to the snow surface), under ice pressure sensor, and temperature string. Detailed description can be found elsewhere (Polashenski et al. 2011). The model number deployed was 2010I.

The buoy deployments were scheduled for a two-day period spanning from 13 to 14 August 2012. The description in this section refers to local Alaskan time (UTC - 9 h), to match the circadian rhythm of the cruise log annotations. On the first day of deployment (August 13), the weather and visibility were good and a number of systems were deployed, however thick fog rolled in overnight and the next morning (August 14) the visibility was very poor. With conditions barely improving and our deployment window shrinking, it was decided that the remaining systems should be deployed relatively close to the ship, but on different ice types, i.e., a combination of FYI and MYI. In this way we could investigate the differential movement between

the deployed systems should the floe deform, as well as the differential melt processes that occur within a single floe comprised of different ice types.

On August 13, the first set of buoys was deployed at the starboard side of the ship (about 20 m from the ship) on the smooth FYI (Table 1). They included one SATICE (SI03), two IMBs (KP01 and KP08), and one SIMB (2010I). All four buoys were deployed relatively close together (Figure 1d). In order for the melt processes measured by KP01 to be analyzed in conjunction with the complementary data from SI03 the separation between buoys SI03 and KP01 was particularly close, about 6 m. At a distance of around 20 m from these two systems, buoys KP08 and 2010I were deployed for inter-calibration purposes. The ice thickness and snow depth at these deployment locations were similar, 1.09-1.28 m and 0.07-0.10 m, respectively (Table 1). In the evening of August 13, a helicopter photographic survey was conducted for one hour. The aerial photo shown in Figures 1c-1d was taken during this survey.

On the morning of August 14, three buoys were deployed at the portside of the ship, at about 20 m from the ship (Figure 1d). These were SATICE (SI04) and two IMBs (KP02 and KP07). Buoys SI04 and KP02 were also deployed within 6 m of each other, but KP07 was deployed at about 15 m distance from SI04 at the edge of a small melt pond. The ice thickness and snow depth at those deployment sites varied very little at around 1.04 m and 0.11 m, respectively (Table 1).

In the afternoon of August 14 two buoys (KP03 and KP04) were deployed on the MYI; lying at about 100-150 m from the starboard side of the ship (Figure 1d). The ice thickness at the KP03 site was 3.17 m, which was much thicker than the smooth FYI where previous buoys deployed (Table 1). Additional drill-hole thickness measurements nearby to the KP03 site confirmed this thickness, with ice thicknesses up to about 4 m being measured. The location of KP04 was chosen to be at the edge of a small melt pond to try to capture the thermal evolution of this MYI melt pond. Although it was clearly the same piece of MYI the ice thickness, 1.01 m, was much thinner at the KP04 than at the KP03 location. Enhanced thinning at the KP04 site may be seen by the darker tones in the snow cover near KP04 (see Figure 1d).

For the last two buoys (KP05 and KP06) we selected the MYI located about 150 m from the ship, and about 10° from the ship heading (Figure 1d). The locations of KP05 and KP06 were chosen to sample two different ice thicknesses while lying on

the same piece of MYI, i.e., KP05 was deployed in the 3.0-m thick ice while KP06 was deployed in 1.4-m thick ice (Table 1). This highlights the differential melt processes that occur with MYI.

Table 1 contains the details of GPS sampling rates, parameters logged, and operational status of the buoys (as of this writing). Upon leaving the floe all buoys were functioning correctly. However, KP06 and KP01 failed prematurely on August 23 and September 14, respectively, and a series of major deformation events in December (described in section 4) shortened the lives of SI03, SIMB-2010I, KP05, and KP07. Only five buoys (SI04, KP02, KP03, KP04, and KP08) survived these deformation events and all KP-IMB thermistor chains were compromised or lost. Among the buoys that survived the deformation, KP02 was located only about 6 m from SI04, near the center of the FYI floe, KP08 was located in FYI, near the FYI/MYI boundary, and KP03 and KP04 were deployed in MYI (Figure 1d). Because this study focuses on GPS-based positioning, KP02 will not be further utilized as its short distance to SI04 is within the 1-sigma position error of the former (see below). Furthermore, because the GPS position estimates of SI04 are more than two orders of magnitude better than those of the KPs with regard to both precision (few cm versus few m; see below) and sampling rate (30 s versus 1 hr), in this study SI04 acts as the position/velocity ground-truthing anchor for the KP-IMB network (see below). Given these details, our floe deformation analysis will use the positioning data from four buoy systems: SI04, KP03, KP04, and KP08 (highlighted in bold in Table 1).

### 3. GPS data, methods, and error assessment

We obtained position information with three different observing platforms, each using a different type of GPS receiving system (see Table 1). The first platform, a SATICE buoy, was equipped with a geodetic-quality GPS system. Data processing of dual-frequency GPS (carrier-phase) observables using the high-rate GPS technique, and the resulting position and error estimates are described in Elosegui et al. (2006). Of relevance to this study, position estimates for SI04 were obtained once every 30 s with cm-level precision. On the other hand, the two other platforms, i.e., the IMBs and the SIMB buoys, were equipped with single-frequency code GPS receivers. The same GPS system was used in the 8 IMB (KP) buoys, but different, in turn, from the SIMB GPS unit. Position estimates from the single-frequency systems

were obtained once per hour (though other sampling times were also used; see Table 1), with a precision that is 2-3 orders of magnitude worse than the geodetic-quality GPS counterpart, or at the few-m level. Since the focus of this study is the use of position estimates from the combined GPS network to measure floe deformation, we turn next to the data, methods, and error assessment with emphasis on the low-precision GPS systems.

GPS data in applications that involve low-precision receivers such as those in the IMB and SIMB buoys typically refers to position estimates, which are readings provided directly by the receiver. In contrast, GPS data from geodetic-quality systems refers to the carrier-phase (raw) observables, which require data post-processing using precise GPS satellite products and state-of-the-art geophysical models and optimal estimation methods to obtain high-precision position estimates. Hereafter, for consistency among GPS systems, we will use GPS data when we refer to position estimates. Although GPS data in these lower-grade receivers are specified to the equivalent of about 10 cm, the precision is significantly worse. Moreover, error estimates are commonly missing, which hampers GPS data editing and validation. Since the scientific focus of this study is floe deformation over small (between 110- 250 m) spatial scales using GPS data from a relatively fast-moving (up to about 0.7 m/s) network, error assessment becomes essential.

Before assessing the errors, we formed a dataset of horizontal baselines (i.e., horizontal component of baseline length and baseline orientation) with the data of all IMBs by subtracting the position at each IMB epoch from the corresponding horizontal position of SI04. Theoretically, the position error of each GPS system should be smaller than the baseline error. Therefore, the estimated baseline error should be an upper bound for the GPS error of each system. In practice, SI04 does not contribute to the baseline error because the variance of the IMB GPS data is about  $10^4$  times larger than the variance of the SI04 data, thus effectively making the latter a “ground-truth” estimate for the IMB GPS data. An additional benefit of using SI04 as baseline reference is that its high-precision data are also high rate, i.e., are estimated here once every 30 s. This is a very desirable feature because it provides a regularized time axis against which the IMB GPS data, whose time stamps may not be regular (see Table 1) nor necessarily coincide with those of SI04, can be aligned prior to forming the baseline dataset without introducing any significant error.

We used a simple linear model to align the IMB GPS data to the epoch of the closest SI04 estimate. Velocities for the linear model are calculated by differentiating the 30-s position estimates of SI04, thus resulting in velocity errors that are smaller than  $1 \text{ cm s}^{-1}$ . For 30-s sampling, alignment involves epoch differences that are always less than 15 s. Propagating the velocity errors through the linear model thus results in alignment errors that are cm level, or negligible. It is explicit in the error calculation above that the floe does not rotate appreciably during the time interval involved in the alignment, which is a reasonable assumption. Indeed, it can be easily calculated that for the longest (209 m) baseline in our network and largest (15 s) time sampling difference between an IMB and SI04, a position error (5 m) that is commensurate with the error of the IMB GPS data would result from a floe rotation of  $329^\circ$  per hour, which is unrealistic (see below). Once the linear interpolation had been applied the baseline length ( $L$ ) and orientation ( $\theta$ ) of three IMBs (KP03, KP04, and KP08) were calculated relative to SI04. The baseline orientation is defined positive east from north, i.e., clockwise, thus consistent with the definition of a topocentric frame centered on the position of SI04.

To estimate baseline error, we calculated the root-mean-squared (RMS) scatter around the mean length of two baselines, SI04-KP03 and SI04-KP08, for the month of November 2012, a month during which the floe did not deform. The RMS values are 1.7 and 3.6 m for baselines SI04-KP03 and SI04-KP08, respectively, while the RMS value for SI04-KP04 was significantly larger, about 8 m (Figure 2). The difference between baselines seems to be related to GPS sampling rate, among other factors. For example, the GPS sampling rate of KP03 and KP08 in November 2012 was set at 12 h, while the GPS sampling rate of KP04 was set at 1 h (see Table 1). Larger RMS for SI04-KP04 can be attributed to the significant number of outliers (Figure 2a), which is not the case when the GPS sampling is 12 h. Similarly, a large number of outliers are present in the KP03 and KP08 data before November 2012 when the GPS sampling rate was 1 h. The causes for this are not fully understood. To estimate the baseline error, we remove  $3\sigma$  outliers and fitted a Gaussian model to the data (Figure 2b). The  $1\sigma$  (standard deviation) estimates from the Gaussian fit is 3.7 m, which is commensurate with the values estimated for baselines SI04-KP03 and SI04-KP08 for the same period. Thus, we will use an estimated baseline error  $\sigma_L$  of 5 m throughout this manuscript.

The errors for baseline orientation  $\sigma_\theta$  can be estimated by  $\sigma_\theta = \sigma_L / L$  for each baseline L and the baseline error  $\sigma_L$  of 4 m, i.e., the shorter the baseline becomes the larger the errors. The errors in the area calculation  $\sigma_A$  can be estimated by

$$\sigma_A = \frac{1}{2} \sigma_L (L_1^2 + L_2^2)^{1/2} \text{ the array area formed by two baselines } L_1 \text{ and } L_2.$$

## 4. Results

Figure 3a shows that the baseline length L for SI04-KP03 (blue), SI04-KP04 (green), and SI04-KP08 (red). The scatters mostly remain within the 1- $\sigma$  of the baseline error  $\sigma_L$  (shown as dashed lines in the figure) from their deployment in August until a series of deformation events occurred in mid-December. This clearly indicates no deformation of the floe occurred within the summer melt period (August to October), until December 13. There was however significant variability in the rotation (changes in orientation  $\theta$ ) of the floe between the deployment and October (Figure 3b). After mid-October the variability in  $\theta$  of the buoys decreased significantly. This change from pre-October to post-October is most likely associated with the timing of local freeze-up near the buoy location (see Section 5.1 for the details). It is also interesting to see that during the post-freeze-up phase there is an underlying, slow, clockwise rotation to  $\theta$ .

The most interesting aspect of Figures 3a and 3b is the major shift, or step-change, in L and  $\theta$  that occurred in three discrete periods during mid to late December 2012. It is these events, which all occurred within a 10-day period, that are the main focus of this study. The deformation events (D) commenced on December 13 (D13), December 16 (D16), and December 21 (D21). Between each of these deformation events L and  $\theta$  remained relatively constant suggesting that the deformed floe remained in a stable state (Figure 3c). The location of each of the three deformation events (D13, D16, and D21) is labelled in Figures 3c and 3d.

The drift track and speed of the floe for the month of December, calculated by differentiating the high-precision position data of SI04 in time, can be seen in Figure 4. During this month the floe drifted about 275 km, performing an elliptical shaped drift that eventually transported the floe very close to its initial position at the start of the month (Figure 4). During this time the drift of the floe went through a number of increases and decreases in drift speed with the average speed being 0.10

$\text{m s}^{-1}$ , a standard deviation of 0.06 ( $N = 89277$ ), and maximum and minimum speed of about  $0.4 \text{ m s}^{-1}$  and  $0 \text{ m s}^{-1}$ , respectively. We now briefly summarise the environmental parameters and ice dynamics during these three deformation events.

#### 4.1. The D13 event

The first deformation event (D13) occurred between 17:00 UTC on December 13 to 06:00 UTC the following day (December 14), a total of 13 hours. During this 13-hour deformation episode the floe drifted at a fairly uniform speed ( $0.13 \text{ m s}^{-1} \pm 0.006$ ,  $N = 1560$ ) and heading ( $-89.87^\circ \pm 5.49$ ,  $N = 1560$ ) (Figure 5a), as calculated from the SI04 data. Meteorological measurements obtained once every 10 min by SI04 showed that air temperature during this period was fairly constant at  $-32.2^\circ \text{C}$  ( $\pm 0.4$ ,  $N = 79$ ) (Figure 5b), the air pressure was dropping slightly at around 994.7 hPa ( $\pm 0.8$ ,  $N = 79$ ) (Figure 5c), and the humidity also remained constant at 76.3 % ( $\pm 0.2$ ,  $N = 79$ ) (not shown here).

This deformation event displaced buoys KP03, KP04, and KP08 relative to SI04. KP03 went through anticlockwise rotation of about 20 degree relative to SI04 but with very little change in L between SI04 and KP03 (Table 2). Similar anticlockwise rotation was shown in KP04, but L between SI04 and KP04 was also increased by 22.8 m (Table 2). In contrast, no significant rotation was observed in KP08, yet the baseline between SI04 and KP08 was stretched by 54.2 m (Table 2). If we plot the positions of the buoys before and after the event (Figure 6a: before in white, and after in red) the effects of this deformation event become apparent. Essentially, the buoy array rotated in an anticlockwise direction and it became narrower and more elongated. The area change within the outermost array of buoys SI04-KP08-KP04 was  $1222 \text{ m}^2$  (above area error limit  $\sigma_A$ ), reducing from  $4797 \text{ m}^2$  to  $3575 \text{ m}^2$  (Table 3). This compression event resulted in an almost 26% reduction in ice area.

Upon further investigation, it was found that 2010I, which was deployed beside KP08 (within about 5 m) moved together, while SI03, deployed about 20 m away, moved in a different direction (Figure 6d). This decoupled movement between KP08 and SI03, even though they were initially separated by 20 m, highlights the complex nature of sea ice deformation. Interestingly, some of the largest movements occurred in regions that had a high number of melt ponds in summer. It could be that the now refrozen melt ponds represent regions of thinner

ice, and thus may provide regions of mechanical weakness that fail under sustained compression and shear. Local differences in ice strengths may be a plausible explanation for the differential movement of the buoys.

#### 4.2. The D16 event

The second deformation event (D16) occurred over an 11-hour period, starting at 20:00 UTC on December 16 and finishing at 07:00 UTC on December 17. During this event the average drift velocity was  $0.17 \text{ m s}^{-1}$  ( $\pm 0.02$ ,  $N = 1320$ ) although the floe speed decreased slightly during this event (Figure 4 and Figure 5a). The heading remained almost constant ( $-42.3^\circ \pm 2.9$ ,  $N = 1320$ ) (Figure 4). During this event, there was only slight drop in air temperature ( $-26.9^\circ \text{C} \pm 0.7$ ,  $N = 63$ ) (Figure 5b), the air pressure also dropped slightly ( $996.7 \text{ hPa} \pm 0.2$ ,  $N = 67$ ) (Figure 5c), and so did the humidity ( $79.5\% \pm 0.4$ ,  $N = 67$ ) (not shown here).

The D16 event can be characterized mainly by a slight stretching in the baselines length ( $\Delta L_s$ , 8–11 m) and rather uniform clockwise rotation of  $15 - 23^\circ$ . The clockwise nature of the deformation process changed the shape of array. The array became much narrower and was stretched along the baselines direction followed by the previous D13 event, which indicates a relaxation of the ice after the D13 deformation event. Interestingly, this clockwise rotation carried the buoys back towards their position prior to the D13 event (Figure 6e). The decoupled nature of the movement of the buoys shown during the D13 deformation event also occurred during the D16 event. The movement of SI03 was again decoupled from KP08 and 2010I (Figure 6e). Both KP08 and 2020I co-rotated by about 15 degrees clockwise (above the baseline orientation error limit  $\sigma_\theta$ ), and moved by 12 m, while the location of SI03 remained almost unchanged (within the baseline length error limit  $\sigma_L$ ) (Figure 6e). This, again, highlights the non-linear nature of small-scale ice deformation.

#### 4.3. The D21 event

The final deformation event, D21, occurred almost exactly 8 days after the first deformation event of the floe, and was by far the most destructive. It started at 18:00 UTC on December 21 and ended at 9:00 UTC on December 22, a total of 15 hours. (The period of D21 event is defined to capture the most dramatic deformation. It should be noted that  $L$  increased about 10 m ( $\Delta L$ ) after the D21 event and then shrank back over a day after the event.) This event destroyed several

of the platforms that were deployed and were operational on the floe. SI03, KP05, and 2010I were completely destroyed and the ice mass balance component (thermistor chain installed within the ice) of buoys KP03, KP06, KP07, and KP08 were lost, but the GPS component of these buoys continued to work (see Table 1). Miraculously, only SI04 did not suffer any loss of sensors although it was deployed very close to KP07 (within 6 m), who also lost its mass balance chain.

The environmental parameters surrounding the D21 event are particularly interesting. A significant drop in surface pressure, by almost 30 hPa (Figure 5c), was accompanied by a corresponding rise in air temperature and humidity (Figure 5b), indicating a passage of a low pressure system at the buoy location. The air temperature rose very quickly from -31°C at 18:06 UTC on December 21 to -21°C at 09:06 UTC on December 22, and by the end of the day the temperature rose almost to -8°C (Figure 5b). During this time the air pressure dropped significantly from 1031.5 hPa at the start of the event to 1015.1 hPa at the end of the event (Figure 5b), and the humidity was also increased from 76.7 % to 82.2 % (not shown here). These represent some of the largest changes the SI04 system recorded between August 2012 and the end of May 2013.

In the days prior to D21 the floe performed two very tight turnings in the drift pattern (in direction of almost 300°) (Figure 4). The last change in direction occurring less than 12 hours before the deformation commenced. During the deformation period the drift direction remained constant at -67° ( $\pm 4$ ). However, the drift speed of the floe accelerated, increasing from near 0.1 m s<sup>-1</sup> to over 0.3 m s<sup>-1</sup> at the end of the event (Figure 4 and Figure 5a). The average drift speed during D21 was remarkably fast at 0.25 m s<sup>-1</sup> ( $\pm 0.07$ ).

During this 15-hour deformation event we witnessed a catastrophic failure of the integrity of the floe. Significant movement occurred at all buoy sites (Figure 6f). The SI04-KP03 baseline length decreased from 179.3 m to 84.8 m ( $\Delta L = -94.5$  m), SI04-KP04 decreased from 248.7 m to 106.7 m ( $\Delta L = -142.0$  m), and SI04-KP08 decreased from 169.7 m to 67.3 m ( $\Delta L = -102.4$  m), all well above the baseline length error  $\sigma_L$  (Table 2). To put these changes in context, to their initial baseline lengths, these changes in  $\Delta L$  represent a reduction in baseline distances by at least 50% (Table 2). This indicates the immense compressive forcing that occurred during this dramatic event, which resulted in substantial mechanical redistribution of relatively thicker sea ice through the process of ridge building.

From Figure 6c we can clearly see that KP03, KP04 and KP08 were all pushed more than 100 m towards SI04. It should be noted that because we discuss motions relative to SI04 from a purely kinematic viewpoint, there is an inherent ambiguity about which moved relative to which. Either way, there is no ambiguity about the compressive nature of the event.

These movements transformed the shape of the array from a long, very narrow triangle to a short, almost equilateral triangle (Figure 6c). This corresponds to shrinking of the outermost buoy array (Area A) of almost  $2100\text{ m}^2$  compared to the array area on deployment ( $4797\text{ m}^2$ ), almost 44% reduction of the area (Table 3). If we assume that ice was on average 1 m thick then this event redistributed approximately 2 million kilograms of ice within the region bounded by the buoys. (Note this area change  $\Delta A$  is well over the area error limit  $\sigma_A$ ).

Again, the differential nature of deformation can be seen through the very different movements of the buoys on the floe. KP08 and KP03 that were very close together (7.4 m) after the previous D16 event moved significantly apart (68.1 m) during the D21 event (Figure 6f).

## 5. Discussion

### 5.1. Freeze-up at local and basin scale

The dynamics of the sea ice is balanced between the inertia, air and water stress on its upper and lower surfaces, the Coriolis force, sea-surface tilt, and internal ice stress gradient (e.g., Hunkins, 1975; Steele et al., 1997). These spatially and temporally varying forces influence internal ice stress that causes deformation within ice field. The internal ice stress on a free drifting floe in summer (a time of low compactness) is very different from that of a floe constrained by winter pack ice. If we are to better understand the nature of some of the above mentioned forces and associated deformation, it is important to understand how the consolidation of ice proceeded (i.e., freeze-up) both at local spatial scales near the buoy location as well as at large basin scales (covering pan-Arctic).

#### 5.1.1. Local freeze-up

The buoys were deployed in late summer when the ice pack is particularly open, so the drift of our instrumented floe more resembles a ‘free drift’ scenario. Local

freeze-up at the buoy location marks the transition of ice conditions from a loosely dispersed assortment of ice floes to a near-continuous ice sheet in the surrounding area. A time-series of high-resolution TerraSAR-X (TSX) Synthetic Aperture Radar (SAR) images acquired in the region near the floe location from late August 2012 to late October 2012 clearly visualize this transition (Figure 7a to 7c). On 29 August 2012, the TSX SAR image shows that individual ice floes (brighter tone) are not consolidated together and open water (much darker tone) exists in between floes (Figure 7a). TSX SAR image on 2 October 2012 shows the formation of new ice between the existing multiyear ice floes (new ice can be identified as darker tone surrounding brighter toned multiyear ice floes) (Figure 7b). The high backscatter in some regions of the image indicates the possible formation of frost flowers over the young active growing ice (Isleifson et al., 2010). The 25 October 2012 TSX SAR image shows much more consolidated ice condition with almost no open-water area in the region (Figure 7c).

This ice formation and consolidation scenario seen by the SAR imagery reasonably agrees with environmental and dynamical information provided by the buoys on the floe. In the month preceding October 15, the air temperature remained above -10 °C and the drift speed of the floe was 0.20 m s<sup>-1</sup> on average. In the month after October 15, however, the air temperature began to drop below -10 °C and ice drift speed decreased to 0.17 m s<sup>-1</sup>, a decrease of 0.03 m s<sup>-1</sup>. Although dropping in air temperature after October 15 qualitatively confirms the timing of local freeze-up, determining the freeze-up based on changes in ice drift speed is not robust as the standard deviation of ice drift speed is quite high at 0.1 m s<sup>-1</sup>.

A more sound determination of local freeze-up can be found from the floe rotation (change in baseline orientation  $\Delta\theta$ ), because the rotation of a floe in free drift would be higher than in a floe in the region of consolidated pack. We estimated the variation of the floe rotation using the techniques developed by Mardia (1972). It measures the dispersion of a directional dataset  $r$ , where  $r = 1$  implies all data is coincident and  $r = 0$  implies uniform dispersion (i.e., smaller  $r$  means larger variance in direction). Using this method, we found the dispersion  $r$  was significantly lower before freeze up ( $r = 0.73$ ) than after freeze up ( $r = 0.99$ ). Given this fact and combined with the TSX SAR analysis, it is very likely that the sea began to freeze early to mid-October near the buoy location, and was well advanced by the end of October.

### 5.1.2. Basin-scale freeze-up

In the above section we described local-scale freeze-up as the timing when sea ice near the floe location became consolidated together. During this period (mid-October) sea ice edge did not extend into the coastal line in the Pacific Sector of the Arctic, yet there were still significant open water areas existing between the ice edge and the coastal line (not shown here). Considering that compressive sea ice strength can be built up as winds pushed the ice against or along the coastal line (Tremblay and Hakakian, 2006), the timing when sea ice cover is consolidated to the coastal line is an important factor. Pan-Arctic SIC maps show that the basin-scale freeze-up occurred about two weeks prior to the deformation events, roughly between late November and early December 2012.

The internal ice stress  $\sigma_i$  is proportional to wind stress  $\tau_a$  and fetch  $L_f$ , i.e.,  $\sigma_i \sim \tau_a \times L_f$  (Tremblay and Hakakian, 2006). Thus, the effects on basin-scale freeze-up on internal ice stress (and resulting deformation) are discussed in these two factors. For the effects of wind stress, we first look at the mean sea level pressure (SLP) pattern during December 2012. The pressure pattern shows the characteristics of strong negative phase of the Arctic Oscillation (AO) (Figure 8a), i.e., higher SLP in the high Arctic. Associated with this mean SLP pattern, the ice motion in the Beaufort Sea and Chukchi Sea was mainly southward toward the coast. In contrast to the mean SLP pattern, during the three deformation events the pressure pattern exhibited the occurrence of low-pressure systems (Figure 8b-d), and the associated ice motion was also quite different as well (Figure 9a-c). During both D13 and D16 events, the pattern is characterized by a strong low-pressure system in the East Siberian Sea (associated with strong cyclonic ice motion). During the D21 event the centre of the low-pressure system was shifted more toward inland of the East Siberia than the other two cases.

At the floe location (marked as a red circle in Figure 9), all the three cases are characterized by northward ice motion, accompanied with the passage of a low-pressure system. The passage of a low-pressure system will influence the local characteristic of ice drift in the region and, in turn, will produce variability within internal pressure field that is dependent on the spatial distribution of ice properties in that particular drift direction. This is the most obvious during D21 in which large-scale ice motion shows strong northward ice motion all the way from the Alaskan coast to the floe, whilst north of the floe the ice motion becomes weaker (Figure 9c).

This suggests that the presence of sea ice pack to the north is inhibiting the northward ice motion. Another factor to consider is the length of fetch  $L_f$  over which wind stress is applied across the surface of the sea ice cover. Once sea ice forms continuously across the basin, it would increase effective  $L_f$  significantly. Recall the deformation events occurred about two month after local freeze-up, and about two weeks after the basin-scale freeze-up. This would allow sufficient time for sea ice to grow thicker and mechanically rigid, forming a continuous ice field around the floe, like a mechanical continuum.

The results indicate that both large-scale wind pattern (ice motion) and basin-scale ice freeze-up would have impacts on the internal ice stress, and thus the small-scale deformation events. It should be noted that this is mainly based on a limited number of cases and also based on qualitative evaluation. More quantitative and robust relationship between large scale winds and internal ice stress (deformation) requires further investigation. For example, including new parameters such as horizontal gradient of ice motion, ice thickness, and ice temperature distribution should be considered, rather than simply correlating basin-scale mean wind stress with deformation.

## 5.2. Strain rate

Schluson (2004) estimated that the ductile-to-brittle transition strain rate was as low as the order of  $10^{-8} \text{ s}^{-1}$ . This relatively low transitional value was attributed to larger stress concentrators normally found in sea ice (e.g., cracks, leads, and refrozen melt ponds at the length scale of 100 m). Our case also resembles ice condition that is highly heterogeneous (horizontal thickness variation), composed of stress concentrators such as refrozen melt ponds and cracks created by the ship track (Figure 1d).

To estimate strain rate, we used the pairs of buoys, as opposed to use multiple buoys to calculate full sets of deformation (see Hutchings and Hibler, 2008). The reasons are:

- a) by using multiple buoys, GPS errors from the IMBs ( $\sim 5 \text{ m}$ ) get further amplified and become too large to estimate deformation over a small array ( $< 3 \text{ km}^2$ ) (Hutchings et al. 2012), and
- b) GPS sampling times between IMBs were not synchronized, which can also contribute to increasing the error due to the time difference. By focusing on

the sets of IMBs paired with the geodetic-quality (cm accuracy) GPS buoy (SI04), we can minimize the propagation of GPS errors in calculation of deformation rate.

We thus calculated one-dimensional (natural) strain rate  $\varepsilon_L$  along the baseline length L defined as

$$\varepsilon_L = V_L(t) / L(t) \quad (1),$$

where  $V_L = [dL(t+dt) - L(t)] / dt$ .

Here  $V_L$  is the rate of change of the baseline length  $\Delta L$  at time t. This is similar to that which was used in Rampal et al. (2008) who estimated the dispersion of pairs of drifters, although we use natural strain as opposed to Lagrangian strain (i.e., measure change in baseline length relative to the initial baseline length). Note that being one dimensional strain rate,  $\varepsilon_L$  cannot distinguish between divergence and convergence from shear. For large deformations ( $> 15\%$ , as in our case), the natural strain is more appropriate.

More explicit deformation rate can be calculated for each pairs of buoys in a two-dimensional space having SI04 as the reference of the coordinate system. Assuming that velocity is constant within the time scale, the two invariants of the deformation, the divergence  $\varepsilon_d$  and shear strain  $\varepsilon_s$ , can be calculated from velocity vectors as:

$$\varepsilon_d = u_x + v_y \text{ and } \varepsilon_s = \left[ (u_x - v_y)^2 + (u_y + v_x)^2 \right]^{1/2} \quad (2).$$

The magnitude of the total deformation  $\varepsilon_t$  can be obtained by:

$$\varepsilon_t = \left[ \varepsilon_d^2 + \varepsilon_s^2 \right]^{1/2} \quad (3).$$

Figure 10 shows the temporal variability of the calculated deformation rates ( $\varepsilon_L$  (black),  $\varepsilon_d$  (blue),  $\varepsilon_s$  (green),  $\varepsilon_t$  (red)) for the two pairs of buoys, SI04-KP03 and SI04-KP08, spanning the deformation events. Deformation rates were calculated at the time scale of 12 h, which was the maximum GPS sampling rate set by both KP03 and KP08 during this period (Table 1). We did not use KP04 for the strain rate calculation as it shows much larger GPS errors than KP03 and KP08. Total strain rate calculated from SI04-KP04 at the 12-h time scale shows the magnitude similar to the ones from SI04-KP03 (not shown here).

Hutchings et al. (2012) presents an error analysis in calculation of strain rate for multiple buoys (see Eq. A4 in their paper). We adapted their error estimation into our case, in which the strain error ( $\sigma_\epsilon$ ) can be estimated as:

$$\sigma_\epsilon = \sqrt{2}\sigma_{gps} / TL \quad (4),$$

where GPS error ( $\sigma_\epsilon = 5$  m), GPS sampling rate (T) and baseline length ( $L = 100$  m).

The estimated strain rate errors are  $1.9 \times 10^{-5}$ ,  $3.2 \times 10^{-6}$ , and  $1.6 \times 10^{-6} \text{ s}^{-1}$  for  $T = 1, 6,$  and  $12 \text{ h}$ , respectively. These are shown in Figure 10 as horizontal, grey dash-dot lines. As can be seen in the Figure, strain rate errors are larger than the deformation signal, except for the D21 event, at the 1-h GPS sampling rate, but strain rate errors become sufficiently small when we compared to our observations for GPS sampling rates of 6 hours and slower.

Strain rate  $\epsilon_L$  estimated from baseline length is consistently lower than total deformation rate  $\epsilon_t$  by a factor of 4. Similar relation between strain from dispersion and total deformation rate was observed in Rampal et al. (2008). The three events are clearly distinctive by peaks in total deformation  $\epsilon_t$ , which is within the range of the order of  $10^{-5} \text{ s}^{-1}$  at the 12-h time scale (Figure 10). This value is larger than the transitional value ( $10^{-8} \text{ s}^{-1}$ ) estimated by Schulson (2004), but is smaller than the value ( $10^{-4} \text{ s}^{-1}$ ) used in Marsan et al. (2004).

A wide range of ductile-to-brittle transitional strain rates (ranging from  $10^{-8} \text{ s}^{-1}$  to  $10^{-4} \text{ s}^{-1}$ ) has been reported in the literature (Schulson, 2001 and 2004; Sodhi, 2001). The main reason for the existence of such a wide range of the transitional values is due to different length scale for the stress concentrators (i.e., cracks/leads) at different spatial scales. The original model equation to estimate the ductile-to-brittle transitional strain rate was based on micro-scale laboratory experiments, and then the transitional value for the large-scale sea ice fracture was estimated from the same model and parameters across the scale except the length scale of stress concentrator d, like cracks/leads in sea ice. Figure 11 illustrates how the brittle transitional strain rate estimates vary with the length scale of stress concentrators. It is interesting to note that the transitional strain rate is of order of  $10^{-8} \text{ s}^{-1}$  for the range of the length of 200 m ( $d = 200 \text{ m}$ ), but quickly increases when the length scale become smaller than 100 m. This demonstrates that statistics of cracks/leads is important to understand the brittle failure of sea ice. In our experiment, the range

of brittle fracture strain rates that we observed matches with the model estimation by Schulson (2001) for the length of stress concentrators of about 5 m ( $d \approx 5$  m).

Marsan et al. (2004) applied multi-scaling extrapolation to meter scale, and estimated about 15% of the deformation is larger than  $10^{-4}$  s<sup>-1</sup> at the 3-day time scale, implying over 0.2% of the total area. On the other hand Kwok (2001) estimated the brittle failure strain rate of  $10^{-7}$  s<sup>-1</sup>, for the same time scale, accounts for 1% of total deformation of a day. As we discussed above, the brittle strain rate is highly dependent on spatial scale, and thus those estimates of how much brittle failure would occur needs to be examined with caution.

For the temporal scale, the studies mentioned above used satellite derived data (i.e., products from the Radarsat Geophysical Processor System, or RGPS), and have 3-day time steps. It is important to note that our deformation events would remain undetected at 3-day time scales. To examine this, we lowered the time scale from 12 hours to 2 days and calculated total strain rate  $\dot{\epsilon}_t$  accordingly. The results for the time scale of 2 days (black line), 1 day (green line), and 12-h (red line) are shown in Figure 10c. The strain rate for 1-day time scale clearly fails to detect the D13 and D16 deformation events, and for the D21 event it is still above the strain error but reduced by half compared to the 12-h sampling (Figure 10c). For the 2-day time scale, the strain rate become too small and none of the deformation events could be detected. This suggests that the satellite data with the 3-day time scale would significantly underestimate the amount of intermittent, small-scale brittle failure of total deformation.

### 5.3. Atmospheric forcing

To examine the effects of atmospheric forcing we used surface 10-m wind data from ERA Interim reanalysis of the European Centre for Medium-Range Weather Forecasts (ECMWF), obtained from the British Atmospheric Data Centre (BADC). We first extracted the 6-hr surface wind data that was nearest to the GPS location of the floe at each time step (maximum distance between the GPS location and nearest grid point was less than 40 km), and then calculated the magnitude of wind components (wind speed) for November and December months which is shown in Figure 6d. The figure shows that the strong wind (above 10 m/s) occurred during each deformation event, but even stronger wind events also occurred in mid-November (although the start of local freeze-up commenced about a month earlier). Then one

can ask a question why we did not see the deformation at our instrumented ice floe during other strong wind events. To answer this question we examine the force balance of the particular ice floe on which the buoys were deployed.

It has been shown that the force balance of sea ice in the Arctic Ocean away from the coastal areas and in autumn and winter can be described by three components; wind stress  $F_a$ , water drag  $F_w$ , and internal ice stress gradient  $F_i$  as  $F_a + F_w + F_i = 0$  (e.g., Hunkins, 1975; Steele et al., 1997). As water drag  $F_w$  and internal stress gradient  $F_i$  are both directed to the opposite to the ice velocity vector, they act like damping to the magnitude of ice velocity vector (ice speed,  $U$ ) without altering the direction of the vector (Steele et al., 1997). This is the main reason why ice speed is highly correlated with wind speed  $U_a$ , although three forces are balanced. At the time scale longer than a day, the three-force balance is a reasonable assumption (Steele et al., 1997), but at smaller scale (shorter than a day) acceleration (inertia) cannot be ignored (e.g., Weiss, 2013). As we are investigating small-scale deformation in this study, the force balance can be expressed by four force terms as  $F_a = F_w + F_i + A$ , where  $A$  is acceleration. (Note that  $F_w$  and  $F_i$  are always negative but  $A$  is positive or negative depending on the acceleration.) To estimate relative magnitude between forces we first decompose the observed ice speed  $U$  into mean ice speed  $U_m$  and a speed perturbation  $U'$ , as follows,  $U = U_m + U'$ .

Here we view  $U$  as ice speed forced by  $F_a$ , but damped down by both  $F_w$  and  $F_i$ , and also accelerated (or decelerated) at  $A$ . This can be written as:

$$U = U_a + U_w + U_i + U_A,$$

where  $U_a$  is the ice speed forced by  $F_a$ ,  $U_w$  is the ice speed damped by  $F_w$ ,  $U_i$  is the ice speed damped by  $F_i$ , and  $U_A$  is ice speed accelerated at  $A$ . Furthermore each components of  $U$  can be also decomposed as follows;

$$U_a = U_a^m + U_a'; \quad U_w = U_w^m + U_w'; \quad U_i = U_i^m + U_i'; \quad \text{and} \quad U_A = U_A^m + U_A'.$$

$U_m$  represents the mean state, and this can be estimated from the constant ratio ( $U/U_a$ ) if one assumes ocean current is negligible. It should be noted that  $U_m$  technically includes mean state of combined contributions of  $F_a$ ,  $F_w$ ,  $F_i$  and  $A$ , i.e.,  $U_m = U_a^m + U_w^m + U_i^m + U_A^m$ . On the other hand,  $U'$  represents perturbation of combined contributions of  $F_a$ ,  $F_w$ ,  $F_i$ , and  $A$ , i.e.,  $U' = U_a' + U_w' + U_i' + U_A'$ .

We first calculated  $U_m$  by averaging the ratio ( $U/U_a$ ) over 6 hour for the months of November and December 2012, obtaining  $U_m = 0.018 \text{ m s}^{-1} \pm 0.007$

(N=244). This value is comparable to or slightly larger than the values reported in some of previous studies (Shu et al., 2012; Fissel and Tang, 1991; Thorndike and Colony, 1982), although other studies have shown smaller values (Lukovich et al., 2011).  $U'$  was then calculated by  $U' = U - U_m$ . Figure 5e shows the perturbation of ice speeds in the form of kinetic energy (i.e.,  $U'$  multiplied by  $F_a$ ). First note that there are positive peaks in  $F_a \times U'$  (red line). If  $U_m$  reasonably represents mean state, the positive  $F_a \times U'$  indicates relative contribution of excessive acceleration ( $U_A'$ ). For example the very large positive  $F_a \times U'$  during November 9-15 is clearly associated with the oscillatory pattern in which ice floe accelerates upon increased  $F_a$  and decelerates through relaxation as  $F_a$  decreases. It is important to note that  $F_a \times U'$  converges to zero in the absence of  $U_A'$ . In other occasions  $F_a \times U'$  is negative. Note that such negative  $U'$  values can be due to further damping by excessive  $F_w$  and  $F_i$  (i.e.,  $U_w'$  and  $U_i'$ ). If we define the excessive damping as  $U_d'$  ( $U_d' = U_w' + U_i'$ ), the variation of  $F_a \times U'$  can be interpreted as perturbation of relative magnitude between  $U_d'$  (negative) and  $U_A'$  (positive).

Keeping in mind  $U_d'$  is negative and  $U_A'$  is positive, the variation of  $F_a \times U'$  reveals interesting kinetic energy balance. We can see that before December 9 the peaks of high  $F_a$  (high wind events) are associated with the positive  $F_a \times U'$ , meaning the energy gained by  $F_a$  is dissipated through excessive acceleration ( $U_A'$ ) at the floe scale, or by the deformation within thin new ice area at the large scale. As mentioned above very large peaks of  $F_a \times U'$  (red line) occurred during November 9-15 (Figure 5a and 5e). These large peaks clearly indicate significant excessive acceleration of the floe (which can also confirm the potential presence of deformation of ice at the large scale). Particularly note that after the peak on 13 November 2012,  $F_a \times U'$  decreases as it fluctuates at 12-hr cycle. This clearly indicates the effects of inertial motion of the ice floe. Recall local freeze-up began from mid-October 2012 (Section 5.1), so this occurred almost one month after the local freeze-up commenced. Once new ice rigidly forms around the floes (like seen in the TSX SAR images in Figure 7b and 7c), the ice acts like a mechanical continuum, inertial motion of ice pack is significantly reduced. In our case the inertial motion damped down within about 2 days. This is close to the decay scale estimated from mooring data when ice cover was more than 90% (Martini et al., 2014).

A plausible explanation is that new ice surrounded the floe was thinner and more breakable than thicker MYI floes, and under strong wind stress this new ice

was deformed and fractured. As the energy is dissipated through deformation over the new ice, the amount of energy transferred to the ice floe would be significantly reduced, so no deformation observed at the floe. Instead it causes the ice floe to be broken loose from the surrounding ice and perform near-free drift. Once winds subsided, the free drifting ice floe exhibited inertial ice motion in broken ice condition. Another plausible explanation is that the whole ice cover moved in inertial motion. This significantly reduces the energy transfer from wind forcing to the mixed layer (Martini et al., 2014), so no deformation of the floe was observed.

The positive  $F_a \times U'$  ( $U_A'$ ) decreases as we approach December 11, while the negative  $F_a \times U'$  appear on December 11, 14, and 17, meaning excessive damping ( $U_d'$ ) began to play a more significant role. This transition coincides with very sharp decrease in air temperature, to below -30 °C (Figure 5b). The negative  $F_a \times U'$  on December 11 may indicate, in conjunction with the cold temperatures, the thickening of new ice surrounded with the floe. This more compact and thicker ice means the increases in  $F_i$  through ice. However, the immediate effects of more compact and thicker ice on  $F_w$  are not straightforward. This is because the ice-ocean drag coefficient changes over time, i.e., deformation influences the ice bottom geometry and thus affects  $F_w$  (Lu et al., 2011). During the D13 deformation event  $F_a \times U'$  is slightly negative, and deeper negative peaks occur during the D16 event, indicating sudden damping in ice speed (i.e., increase in excessive  $U_d'$ ) (Figure 5e). We cannot confidently say how much these negative peaks were associated with increase between  $F_w$  and  $F_i$ .

On the other hand, the D21 event is characterized by positive peaks of  $F_a \times U'$ . This may suggest that the D21 event differs from the D13/16 events in terms of dynamic characteristics, i.e.,  $U_A'$  vs  $U_d'$ . During the D13/D16 events the drift speed (and environment parameters) were rather stable, while very dramatic changes were observed in ice drift speed (and environmental parameters) during the D21 event (see Section 4 and Figure 4). The wind vectors along the track also depict the characteristics of two different dynamic regimes (Figure 12). During the D13/D16 events, the wind vectors were steady in magnitude and direction, but the wind direction right before the D21 event changed rapidly twice for a total of almost 300°, and then the wind speed increased throughout the event.

The large-scale SLP pattern during the D21 event is also different from those during the two other events. During the D21 event the center of low-pressure

system was located south in the East Siberia (Figure 8d). This caused very strong northward ice motion from the coast of the Chukchi Sea through to the buoy location, but the ice motion was reduced in the north of the floe location (Figure 9c). This creates strong south-to-north gradient in ice motion, which significantly increase internal ice stress in the buoy area. In Figure 5e this shows as increase in excessive acceleration of the floe ( $U_A'$ ) (positive red line), while the D13/D16 events are seen as increase in damping ( $U_d'$ ). We here emphasize that the estimation of the force balance was made at the floe scale, so the results should be understood in the context of both the floe scale as well as large scale. During the D13/D16 events the ice floe was consolidated together with surrounding ice, i.e., a mechanical continuum. Thus the negative  $F_a \times U'$  can be seen as the resistance to the applied  $F_a$ , an increase of internal ice stress  $F_i$  of the ice continuum. On the other hand, the positive  $F_a \times U'$  (excessive acceleration) during the D21 event seems the opposite to what we expected. However, this can be seen as the effects of large-scale deformation and brittle fracturing in the area, which causes cracks for the ice floe to move more freely and accelerate.

Figure 13 contains the TSX SAR images acquired on 25 October 2012 and 23 December 2012. The October 25 image captured sea ice condition at the buoy location before the deformation event (covering an area of 7 by 10 km), yet the December 23 image captured the ice condition right after the D21 deformation event. Note that the December 23 failed to capture the exact floe location, but show the area about 30 km north from the floe location. Here we attempt to see immediate effects of the D21 deformation event. When the two images are compared, the December 23 image clearly shows many fracture lines (thin brighter lines in Figure 13b) which are not shown in the October 25 image (Figure 13a). These lines are mainly shown within the dark-looking new ice area, but in some cases the fracture lines appear across the MYI floe, indicating wide spread brittle fracturing in the area.

## 6. Summary and conclusions

Small-scale (~100 to 200 m) deformations of an Arctic ice floe were observed from multiple GPS buoys deployed on the same ice floe. The types of buoys include a geodetic-quality GPS system (SATICE, cm-level position error) and sea ice mass balance buoys (IMBs) equipped with standard GPS (position error ~5 m). By

pairing with a geodetic-quality SATICE-type buoy, the baseline length and orientation of three IMBs (relative to SATICE) could be estimated with errors that are sufficiently small ( $\sim 5$  m in length and, depending on baseline length, 2 degrees or less in orientation) enough to capture small-scale deformations.

No change in baseline length was detected for the three baselines from the deployment in late August until mid-December 2012. And then both baseline length and orientation changed abruptly during a series of three discrete deformation events (D13, D16, and D21). Each deformation episode lasted less than a day. After the deformation events the baseline length  $L$  between the pairs of buoys shrank by about 50%, and the area covered by the buoy arrays decreased by 40 to 60% at the end of the events, indicating violent compression of the floe (i.e., ridge building). Our observations also showed complex and non-linear nature of the deformation as the buoys separated by only 20 m moved differentially during the deformation.

Satellite imagery and dynamic parameters suggest that the local freeze-up (consolidation of ice near the floe location) occurred at around mid-October, while basin-scale freeze-up (consolidation of ice over the Pacific sector of the Arctic basin) occurred at between late November and early December. Therefore, at the time of deformation, it was already two months into ice growth near the floe location, and about two weeks after basin-scale freeze-up. This allowed enough time for the new ice between multiyear ice floes to be consolidated to form (mechanically) continuous ice continuum. Basin-scale freeze-up also increased the length of ice surface fetch affected by wind stress. In addition, sudden changes in ice motion occurred during the three deformation events. During the deformation events low-pressure systems dominated the SLP pattern which caused northward ice motion toward the floe location and pushing ice against more stagnant pack ice in the north. This is different from the December mean SLP pattern, showing high SLP in the high Arctic. Combination of increased fetch and south-to-north gradient in ice motion increases internal ice pressure and leads to favourable condition for the deformation and brittle fracturing.

Strain rate estimated from the pairs of buoys was of the order of  $10^{-5} \text{ s}^{-1}$  at the time scale of 12 h. This range of strain rate is comparable to the ductile-to-brittle strain rate estimate by Schulson (2001) for the length of crack of 5 m. Actual strain rate would be much larger as the actual deformation could occur much shorter than 12 h. When the time scale lowers to 1 day, even the largest deformation event (D21)

would be underestimated by 50% relative to our measurements. At the 2-day time scale or longer our deformation events could not be detected.

Analysis of force balance reveals the relative effects between internal ice stress gradient  $F_i$  and acceleration  $A$  under atmospheric wind stress. When new ice formed between multiyear ice floes is still thin and weak, strong wind stress was dissipated through deformation/fracturing over the new ice cover. This was shown as (at the floe scale) an increase in acceleration ( $A$ , inertia) of the floe, indicating the ice floe was broken loose from the surrounding new ice and move freely. As colder condition ( $< -30^{\circ}\text{C}$ ) prevailed, the thickness and strength of new ice between the multiyear ice floes increased. Under strong wind stress the internal ice stress gradient  $F_i$  increased through ice cover. (These effects were shown as negative peaks of  $F_a \times U'$  during the D13/D16 events.) This increases  $F_i$  causing the deformation/fracturing which we observed at the strain rate of about  $2 \times 10^{-5} \text{ s}^{-1}$  at our floe location.

However, the most dramatic deformation event, D21, was shown as positive peaks of  $F_a \times U'$ , i.e., acceleration of the ice floe. This can be seen as the effects of large-scale deformation that causes fracturing of surrounding ice cover as well as at the ice floe. This creates fracture cracks for the ice floe to move more freely and accelerate. Low-pressure system during the D21 event was more shifted to the down south in the East Siberia. This caused very strong northward ice motion to the floe location, yet the ice motion in the north is much slower. This sharp south-to-north gradient in ice motion is most evident during the D21 deformation in which we observed most violent compression from our buoy data.

Wide-spread fracturing during these deformation events can be visualized in satellite image (TerraSAR-X ScanSAR) acquired on 23 December 2012 (just 18 hours after the end of the D21 event). The December 23 image failed to capture the exact floe location, but it still shows the sea ice conditions within 30 km from the floe location. Comparing this image with the image acquired on 25 October 2012, it shows many complex fracture cracks mainly in the dark-looking new ice area and sometimes across the multiyear ice floes, indicating wide spread brittle fracturing in the area.

In this study, qualitatively speaking, we see some effects of large-scale wind stress (ice motion) on small-scale deformations. All three deformation events we discussed in this study occurred when low-pressure systems were developed in the

Arctic, a deviation from the December mean pressure pattern. The low pressure systems caused northward ice motion toward the floe location and against stagnant pack ice in the north. This causes very steep south-to-north gradient in ice motion, causing significant build-up of internal ice stress and thus contributing to brittle fracturing. This suggests the kinetic energy gained by wind stress can still be associated with the small-scale deformation to some extent. At the same time, small-scale deformation (at the floe scale) was not observed when surrounding newly formed sea ice was still thin and fragile, as most of kinetic energy by wind stress were effectively dissipated through deformation/fracturing within new ice cover. This suggests that a simple correlation between wind stress and small-scale deformation is difficult to be measured. Exploration of the relationship may require new approach such as using wind stress gradient (not the mean magnitude), and also require additional new parameters such as ice thickness and strength.

## **Acknowledgements**

This work was partly supported by ACCESS, an European Project supported within the Ocean of Tomorrow call of the European Commission Seventh Framework Programme; SATICE, an European Science Foundation (ESF) PolarCLIMATE Programme project; the Marginal Ice Zone (MIZ) Programme by the Office of Naval Research (ONR); the Spanish Ministry of Science and Innovation (MICINN; now MINECO); and the K-PORT (KOPRI, PM13020) project funded by the Ministry of Oceans and Fisheries, South Korea. We acknowledge grateful support from KOPRI, and the captain and crews of IBRV *Araon* during the ARA04B cruise. We also thank engineers Markus Olsson of CSIC and Shane Rodwell, Alistair James, and Bernard Hagan at SAMS for their involvement in SATICE instrument development and deployment. The TerraSAR-X imagery in this project was acquired via DLR TSX SSS project to BJH. ECMWF ERA Interim data were acquired from BADC. SIMB GPS data is publicly available thanks to CRREL. We thank Jennifer Hutchings, and an anonymous reviewer for constructive reviews.

## **References**

- Elosegui, P., Davis, J.L., Oberlander, D., Baena, R., Ekström, G., 2006. Accuracy of high-rate GPS for seismology, *Geophysical Research Letters* 33, L11308, doi:10.1029/2006GL026065.
- Elosegui, P., J. Wilkinson, M. Olsson, S. Rodwell, A. James, B. Hagan, B. Hwang, R. Forsberg, R. Gerdes, J. Johannessen, P. Wadhams, M. Nettles, L. Padman, 2012. High-precision GPS autonomous platforms for sea ice dynamics and physical oceanography, Fall Meeting of the American Geophysical Union, C13E-0662, San Francisco.
- Fissel, D.B., Tang, C.L., 1991. Response of sea ice drift to wind forcing on the northeastern Newfoundland Shelf. *Journal of Geophysical Research* 96 (C10), 18,397-18,409.
- Geiger, C.A., Zhao, Y., Liu A.K., Häkkinen, S., 2000. Large-scale comparison between buoy and SSM/I drift and deformation in the Eurasian Basin during winter 1992–1993. *Journal of Geophysical Research* 105 (C2), 3357–3368.
- Herman, A., Glowacki, O., 2012. Variability of sea ice deformation rates in the Arctic and their relationship with basin-scale wind forcing, *The Cryosphere* 6, 1553–1559.
- Hutchings, J., Roberts, A., Geiger, C.A., Richter-Menge, J., 2011. Spatial and temporal characterization of sea-ice deformation. *Annals of Glaciology* 52 (57), 360–368.
- Hutchings, J.K., Heil, P., Steer, A., Hibler III, W.D., 2012. Subsynoptic scale spatial variability of sea ice deformation in the western Weddell Sea during early summer, *J. Geophys. Res.*, 117, C01002, doi:10.1029/2011JC006961.
- Hunkins, K., 1975. The oceanic boundary layer and stress beneath a drifting ice floe. *Journal of Geophysical Research*, 80(24), 3425-3433.
- Isleifson, D., Hwang, B., Barber, D.G., Scharien, R.K., Shafai, L., 2010. C-Band Polarimetric Backscattering Signatures of Newly Formed Sea Ice During Fall Freeze-Up. *IEEE Transactions on Geoscience and Remote Sensing* 48 (8), 3256–3267.
- Jackson, K., Wilkinson, J. Maksym, T., Beckers, J., Haas, C., Meldrum, D., Mackenzie, D., 2012. A Novel and Low Cost Sea Ice Mass Balance Buoy. *Journal of Atmospheric and Oceanic Technology* doi:10.1175/JTECH-D-13-0058.1.

- Kovacs, A., 1996. Sea ice: Part II, Estimating the full-scale tensile, flexural, and compressive strength of first-year ice. CRREL Rep. 96-11, Cold Reg. Res. and Eng Lab., Hanover, NH.
- Kwok, R., Cunningham, G.F., 2012. Deformation of the Arctic Ocean ice cover after the 2007 record minimum in summer ice extent, *Cold Regions and Technology*, 76-77, 17-23.
- Kwok, R., Rothrock, D.A., 2009. Decline in Arctic sea ice thickness from submarine and ICESat records: 1958 – 2008. *Geophysical Research Letters* 36, L15501, doi:10.1029/2009GL039035.
- Kwok, R., Sulsky, D., 2010. Arctic Ocean Sea Ice Thickness and Kinematics. *Oceanography* 23 (4), 134-143.
- Lu, P., Li, Z., Cheng, B., Leppäranta M., 2011. A parameterization of the ice-ocean drag coefficient, *J. Geophys. Res.*, 116, C07019, doi:10.1029/2010JC006878.
- Lukovich, J.V., Babb, D.G., Barber, D.G., 2011. On the scaling laws derived from ice beacon trajectories in the southern Beaufort Sea during the International Polar Year - Circumpolar Flaw Lead study, 2007–2008. *Journal of Geophysical Research* 116, C00G07, doi:10.1029/2011JC007049.
- Mardia, K.V., 1972. *Statistics of Directional Data*. New York: Academic Press.
- Marsan. D., Stern, H., Lindsay, R., Weiss J., 2004, Scale Dependence and Localization of the Deformation of Arctic Sea Ice. *Physical Review Letters* 93 (17), doi:10.1103/PhysRevLett.93.178501.
- Parkinson, C.L., Comiso, J.C., 2013. On the 2012 record low Arctic sea ice cover: Combined impact of preconditioning and an August storm, *Geophysical Research Letters* 40, 1356–1361, doi:10.1002/grl.50349.
- Petrich, C., Eicken, H., 2010. Growth, Structure and Properties of Sea Ice, In: Thomas D. N., Dieckmann, G. S. (Eds), *Sea Ice*. Second Edition, Wiley-Blackwell, Oxford, UK. doi:10.1002/9781444317145.ch2.
- Polashenski, C., Perovich, D.K., Richter-Menge, J.A. Elder, B., 2011. Seasonal ice mass-balance buoys: adapting tools to the changing Arctic. *Annals of Glaciology* 52 (57), 18-26.

- Rampal, P., Weiss, J., Marsan, D., Lindsay, R., Stern, H., 2008. Scaling properties of sea ice deformation from buoy dispersion analysis. *Journal Geophysical Research* 113, C03002, doi:10.1029/2007JC004143.
- Rampal, P., J. Weiss, J., Marsan, D., 2009. Positive trend in the mean speed and deformation rate of Arctic sea ice, 1979–2007. *Journal of Geophysical Research* 114, C05013, doi:10.1029/2008JC005066.
- Richter-Menge, J.A., Elder, B.C., 1998. Characteristics of pack ice stress in the Alaskan Beaufort Sea. *Journal of Geophysical Research* 103 (C10), 21,817–21,829.
- Richter-Menge, J.A., McNutt, S. L., Overland, J. E., Kwok, R., 2002. Relating arctic pack ice stress and deformation under winter conditions. *Journal of Geophysical Research* 107 (C10), 8040, doi:10.1029/2000JC000477.
- Schulson, E.M., 2001. Brittle failure of ice. *Engineering Fracture Mechanics*, 68, 1839-1887.
- Schulson, E.M., 2004. Compressive shear faults within arctic sea ice: Fracture on scales large and small. *Journal of Geophysical Research* 109, C07016, doi:10.1029/2003JC002108.
- Shu, Q., Ma, H., Qiao, F., 2012. Observation and simulation of a floe drift near the North Pole. *Ocean Dynamics* 62, 1,195-1,200.
- Simmonds, I., Rudeva, I., 2012. The great Arctic cyclone of August 2012. *Geophysical Research Letters* 39, L23709, doi:10.1029/2012GL054259.
- Sodhi, D.S., 2001. Crushing failure during ice-structure interaction, *Engineering Fracture Mechanics*, 68, 1889-1921.
- Steele, M., Zhang, J., Rothrock, D., Stern, H., 1997. The force balance of sea ice in a numerical model of the Arctic Ocean. *Journal of Geophysical Research*, 102 (C9), 21,061-21,079.
- Thorndike, A.S., Colony, R., 1982. Sea ice motion in response to geostrophic winds. *Journal of Geophysical Research* 87 (C8), 5845-5852, doi:10.1029/JC087iC08p05845.
- Tremblay, L.-B., Hakakian, M., 2006. Estimating the Sea Ice Compressive Strength from Satellite-Derived Sea Ice Drift and NCEP Reanalysis Data. *Journal of Physical Oceanography* 36, November, 2165-2172.

- Walter, B.A., Overland, J.E., 1993. The response of lead patterns in the Beaufort Sea to storm-scale wind forcing. *Annals of Glaciology*, 17, 219–226.
- Weiss, J., 2013. Drift, Deformation, and Fracture of Sea Ice: A Perspective Across Scales. Springer Briefs in Earth Sciences, doi: 10.1007/978-94-007-6202-2\_2.
- Zhang, J., Lindsay, R., Schweiger, A., Rigor, I., 2012. Recent changes in the dynamic properties of declining Arctic sea ice: A model study. *Geophysical Research Letters* 39, L20503, doi:10.1029/2012GL053545.
- Zhang J., Lindsay, R., Schweiger, A., Steele, M., 2013. The impact of an intense summer cyclone on 2012 Arctic sea ice retreat. *Geophysical Research Letters* 40, doi:10.1002/grl.5019.

**Table 1** Description of buoy deployment and measurements used in this study.  $H_{\text{snow}}$  and  $H_{\text{ice}}$  denote snow depth and ice thickness in metres respectively. Epoch is DD/MM/YY HH:MM in UTC. The buoy data actually used in the analysis are highlighted in bold in their ID names.

Buoy Type	ID	Deployment Epoch	$H_{\text{snow}}$	$H_{\text{ice}}$	Last GPS reading	Last chain reading	GPS reading interval	Description
High-precision GPS (SATICE)	SI03	13/08/12 23:00	0.07	1.20	21/12/12 17:00	N/A	10 s	Deployed on the level FYI about 20 m from the starboard side of the ship. GPS readings available until 21 December 2012 (D21) event.
	<b>SI04</b>	14/08/12 20:00	0.09	1.06	31/06/13	N/A	10 s	Deployed on the level FYI about 20 m from the port side of the ship. Used as the centre reference point for the baseline and array area analysis. Air temperature, barometric pressure, and humidity measured from this buoy also used in the analysis.
Ice Mass Balance Buoys (IMB)	KP01	13/08/12 23:00	0.10	1.28	14/09/13 22:00	14/09/12 23:00	1 hour	Deployed on the level FYI about 6 m from SI03. Prematurely failed and excluded from the analysis.
	KP02	14/08/12 20:00	0.11	1.06	31/06/13	26/12/12 17:00	-27/10: 1 h 27/10-30/10: 2 h 30/10-12/01: 12 h 12/01-: 1 h	Deployed on the level FYI about 6 m from SI04. Baseline distance within the error range (~5 m), so not included in the analysis.
	<b>KP03</b>	15/08/12 03:00	0.14	3.17	31/06/13	21/12/12 05:00	-05/10: 1 h 05/10-30/10: 2 h 30/10-12/01: 12 h 12/01-: 1 h	Deployed on the MYI about 100 m from the starboard side of the ship. Used for both baseline and area analysis.
	<b>KP04</b>	15/08/12 03:00	-	1.08	31/06/13	27/08/12 12:00	1 h	Deployed on the MYI about 150 m from the ship's starboard side. Used for both baseline and array analysis.
	KP05	15/08/12 05:00	0.05	3.00	11/12/12 16:00	21/12/12 16:00	-05/10: 1 h 05/10-30/10: 2 h 30/10-: 12 h	Deployed on the MYI about 150 m from the ship's bow, GPS lost before the deformation events, not included in the analysis.
	KP06	15/08/12 05:00	0.15	1.43	23/08/12 20:00	21/12/12 15:00	1 h	Deployed on the same MYI with KP04. GPS lost before the deformation events, not included in the analysis.
	KP07	14/08/12 20:00	0.12	1.01	14/12/12 19:00	21/12/12 19:00	-05/10: 1 h 05/10-30/10: 2 h 30/10-: 12 h	Deployed on the smooth FYI about 10 m from SI04. GPS lost before the deformation events, so used as supplementary data.
	<b>KP08</b>	13/08/12 23:00	0.09	1.07	17/04/13 15:00	21/12/12 09:00	-05/10: 1 h 05/10-30/10: 2 h 30/10-12/01: 12 h 12/01-: 1 h	Deployed on the smooth FYI about 20 m from SI03. Used for both baseline and array analysis.
Seasonal Ice Mass Balance Buoy (SIMB)	2010I	14/08/12 03:00	0.10	1.09	21/12/12 20:00	N/A	1 h	Deployed on the smooth FYI about 5 m from KP08. GPS readings available until the Dec 17 event.

**Table 2** Baseline length L and orientation  $\theta$  of deformation events, relative to SI04.  $\Delta L$  and  $\Delta\theta$  are change in L and  $\theta$ , respectively, for the event, and  $\Delta D$  is the buoy displacement. Distances are in meters (m) and angles in degrees ( $^{\circ}$ ). Epoch format is DD/MM/YY HH:MM, in UTC.  $\sigma_L$  and  $\sigma_{\theta}$  are the error estimates for L and  $\theta$ , respectively (see text for definition). SI04 and KP08 are in FYI, KP03 and KP04 in MYI.

Baseline (m)	Epoch	SI04 (FYI) - KP03 (MYI)			SOI4 (FYI) - KP04 (MYI)			SI04 (FYI) - KP08 (FYI)		
		L (m) $\sigma_L$	$\theta ({}^{\circ})$ $\sigma_{\theta}$	$\Delta L$ $\Delta D$ $\Delta\theta$	L (m) $\sigma_L$	$\theta ({}^{\circ})$ $\sigma_{\theta}$	$\Delta L$ $\Delta D$ $\Delta\theta$	L (m) $\sigma_L$	$\theta ({}^{\circ})$ $\sigma_{\theta}$	$\Delta L$ $\Delta D$ $\Delta\theta$
<b>D13</b> <b>(Start)</b>	13/12/12	165.0	325.9	---	211.8	327.2	---	111.5	301.8	---
	17:00	4	1.4		4	1.1		4	2.1	
<b>D13</b> <b>(End)</b>	14/12/12	168.3	306.1	3.3 57.4 -19.8	234.6	309.4	22.8 72.6 -17.8	165.7	298.8	54.2 54.7 -3.0
	09:00	4	1.4		4	1.0		4	1.4	

<b>D16</b> <b>(Start)</b>	16/12/12	168.4	304.6	---	237.7	309.2	---	164.5	295.1	---
	20:00	4	1.4		4	1.0		4	1.4	
<b>D16</b> <b>(End)</b>	17/12/12	180.0	319.6	11.6 42.6 15	246.1	324.1	8.4 62.5 14.9	175.1	317.8	10.6 57.0 22.7
	09:00	4	1.3		4	1.0		4	1.3	

<b>D21</b> <b>(Start)</b>	21/12/12	179.3	320.8	---	248.7	319.2	---	169.7	312.5	---
	18:00	4	1.3		4	1.8		4	1.4	
<b>D21</b> <b>(End)</b>	22/12/12	84.8	298.5	-94.5 105.4 -22.3	106.7	295.6	-142.0 160.6 -23.6	67.3	246.9	-102.4 165.8 65.6
	09:00	4	2.7		4	2.2		4	3.4	

**Table 3** Areas of the buoy arrays on August 14 (17:00 UTC), December 14 (09:00 UTC), December 17 (09:00 UTC), and December 22 (09:00 UTC). The areas on August 14 represent the initial state right after the deployment. The areas on December 14, 17 and 22 represent the state after each deformation event.  $\sigma_A$  is the error estimates for each buoy array (see text for the details).  $\Delta A$  is the change of area before and after each deformation event. Any  $\Delta A$  values above the error  $\sigma_A$  are valid. Note some of  $\Delta A$  becomes smaller or comparable to  $\sigma_A$ .

Date	A SI04-KP08-KP04 Half FYI and MYI		B SI04-KP08-KP03 Predominately FYI		C SI04-KP03-KP04 Half FYI and MYI	
	A ( $m^2$ ) $\sigma_A$	$\Delta A$ ( $m^2$ and %)	A ( $m^2$ ) $\sigma_A$	$\Delta A$ ( $m^2$ and %)	A ( $m^2$ ) $\sigma_A$	$\Delta A$ ( $m^2$ and %)
Aug 14	4797 478	---	3684 398	---	579 536	---
Dec 14	3575 574	-1222 (-26%)	1772 472	-1912 (-52%)	1136 577	557 (96%)
Dec 17	2364 604	-1211 (-51%)	495 502	-1277 (72%)	1738 609	602 (53%)
Dec 22	2697 252	333 (14%)	2236 216	1741 (352%)	229 272	-1509 (-86%)
Total	---	-2100 (-44%)	---	-1448 (-39%)	---	-350 (-61%)

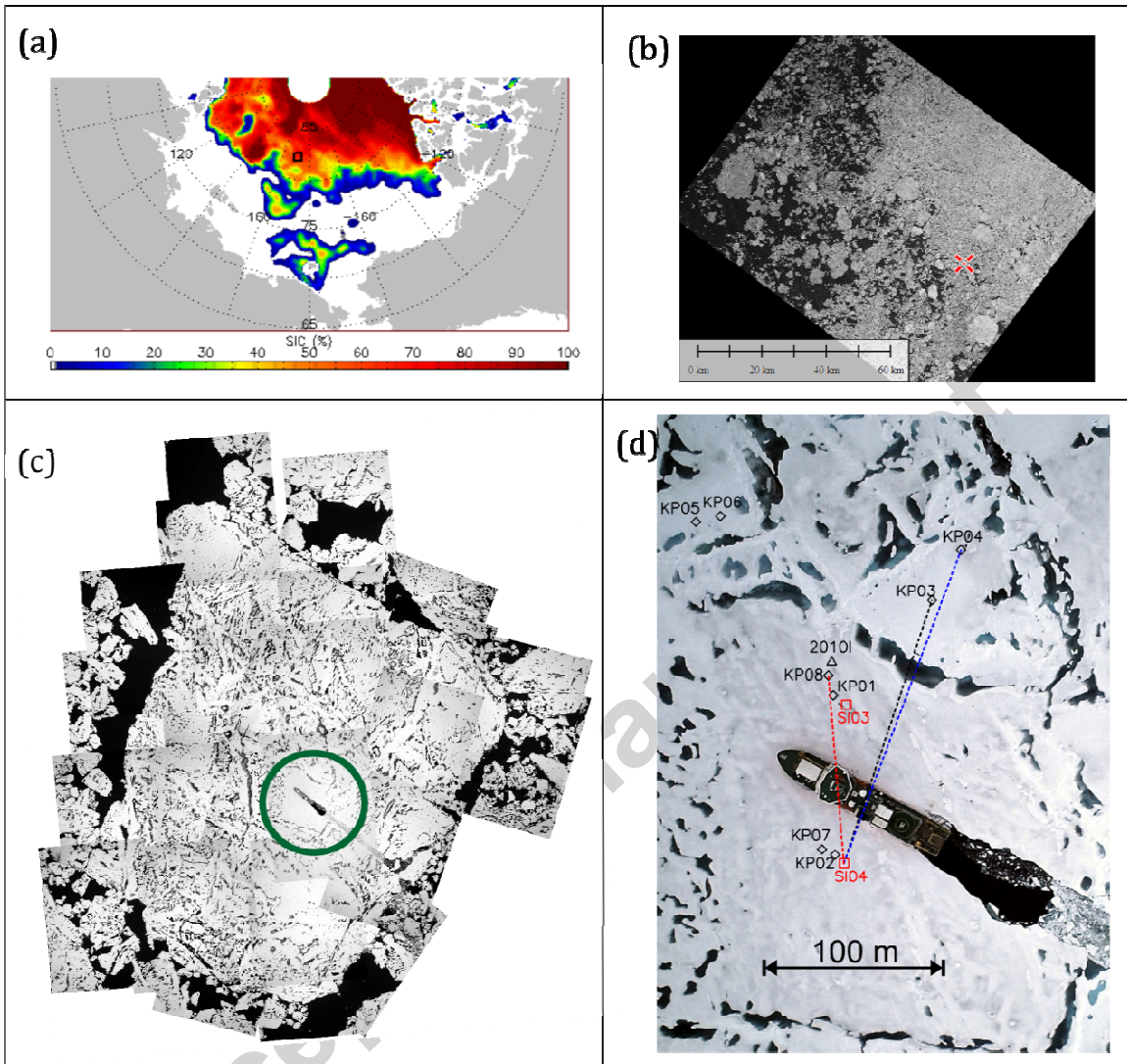


**Figure 1** (a) Sea ice concentration during the buoy deployment, on 14 August 2012, with deployment location marked as a black rectangular box. (b) TerraSAR-X ScanSAR image acquired on 29 August 2012 (15 days after deployment) with floe location marked as a red diagonal crosshair symbol. (c) Aerial mosaic from photos taken on 14 August 2012 but rotated to match the orientation of the floe on 15 August 2012 at 06:00 UTC. The green circle marks the location of IBRV Araon, which is about 100-m long. (d) Zoom in with buoy locations overlaid on the aerial mosaic. In the photo black, blue, and red dashed lines depict baselines to SI04 from KP03, KP04, and KP08, respectively. In all panels, North (East) is direction to the top (right). (See text for more details).

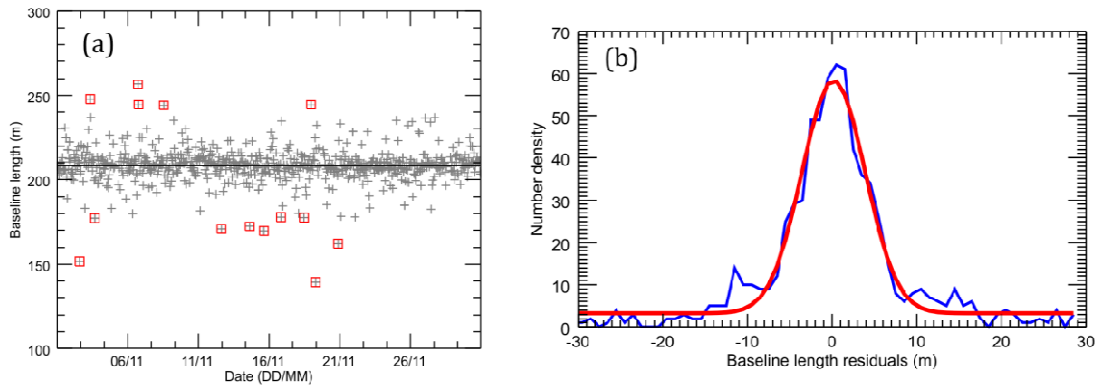


**Figure 2** (a) Times series of SI04-KP04 baseline length estimates in November 2012, with highlighted (red squares) 3- $\sigma$  (standard deviation) outliers. Before and after removing 3- $\sigma$  outliers the mean (and standard deviation) of the baseline length were  $208.4 \pm 10.1$  m ( $N=729$ ) and  $208.6 \pm 8.3$  m ( $N=714$ ), respectively. During this period GPS sampling rate was 1 hour. (b) Number density histogram of the SI04-KP04 baseline length residuals. The blue line is the data histogram of the data points after removing 3- $\sigma$  outliers and the red line is the best Gaussian fit to the data. The mean and standard deviation of the fitted Gaussian are  $-0.2 \pm 3.7$  m ( $N=714$ ).

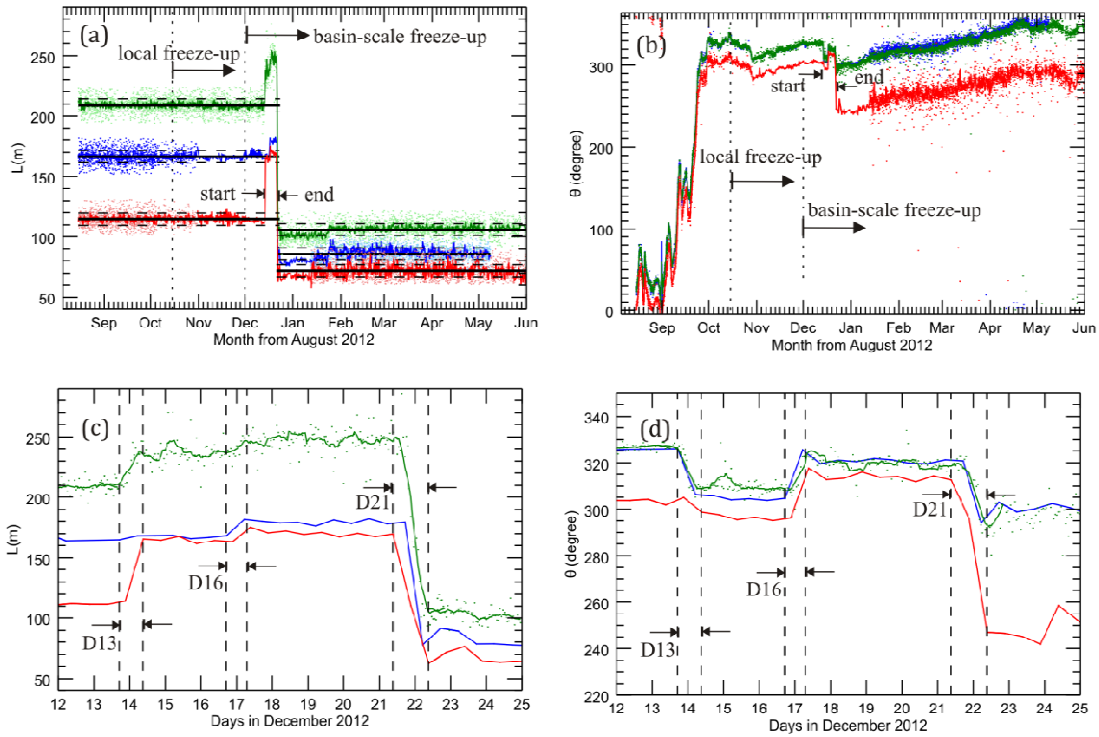


**Figure 3** Time series of (a) baseline length  $L$  and (b) orientation  $\theta$  for the KP03 (blue), KP04 (green), and KP08 (red) baselines to SI04 from deployment in August 2012 through May 2013. In (a) and (c) the small dots are the position data and lines are either data sampled twelve hourly or moving-averaged to 12 hours if the GPS sampling rate was higher than 12 hours (see text). In (a), the black solid and dashed lines are the average and one standard deviation, respectively, during the times of no deformation. Vertical dotted line in (a) and (b) denotes the start of both local and basin-scale freeze-up (see text). Panels (c) and (d) are the same as (a) and (b), respectively, but here for December 2012 to zoom in on the deformation period. Labels D13, D16, and D21 identify the three deformation events.

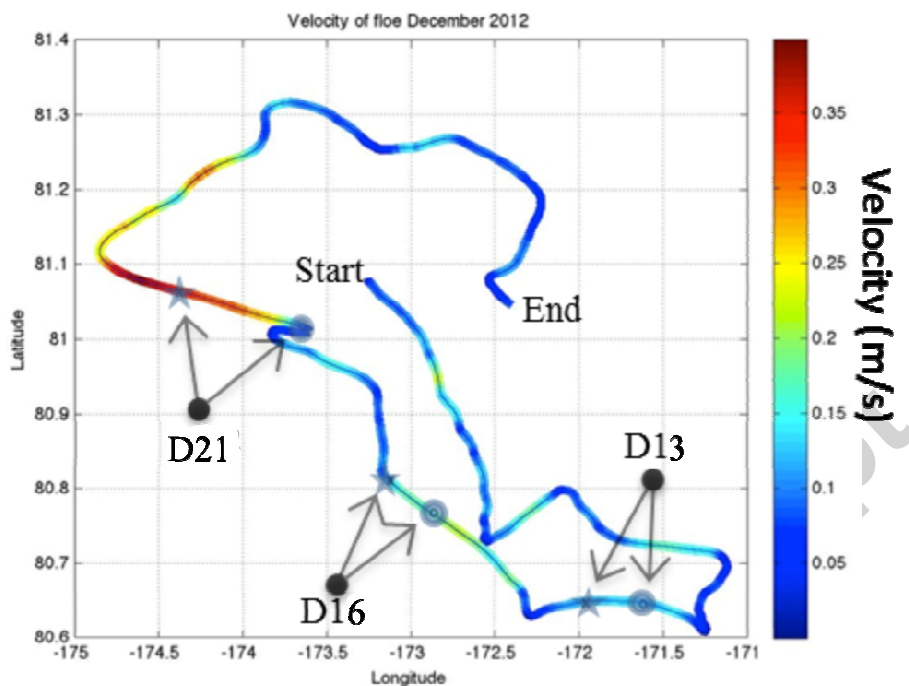


**Figure 4** Drift track of the floe for the month of December 2012. The track is color-coded for drift speed and the locations of these events (D13, D16, and D21) are also displayed. Circle represents the start of a deformation event as seen by a change in baseline distance, and a star represents the finish of an event as seen by the baseline length remaining constant.

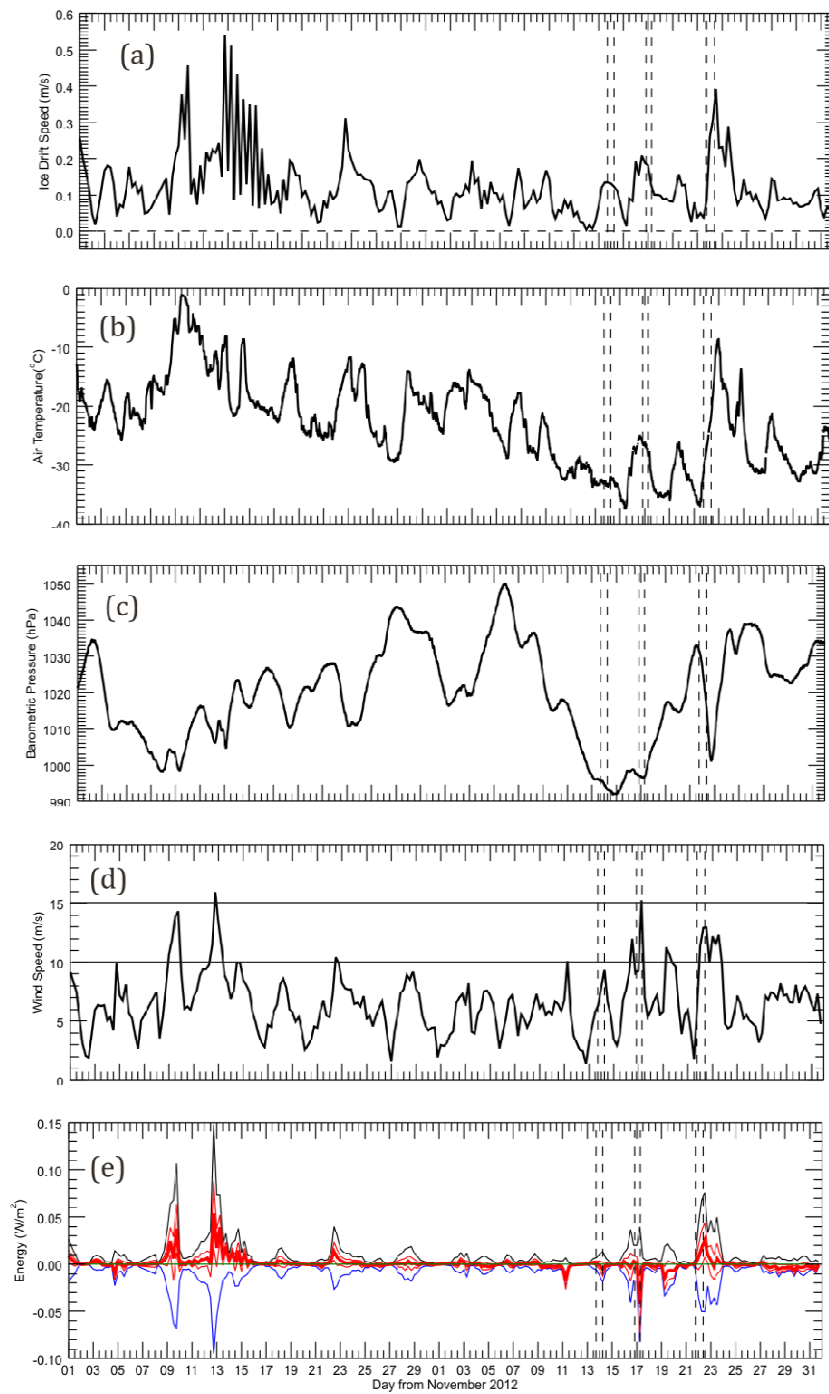


**Figure 5** Temporal variation of (a) ice drift speed, (b) air temperature, (c) barometric pressure, (d) wind speed, and (e) kinetic energy of  $U \times F_a$  (black),  $U_m \times F_a$  (blue) and  $U' \times F_a$  (red), during November and December 2012. Vertical dashed lines denote the times of the D13, D16, and D21 deformation events. (See text for the definition of kinetic energy.)

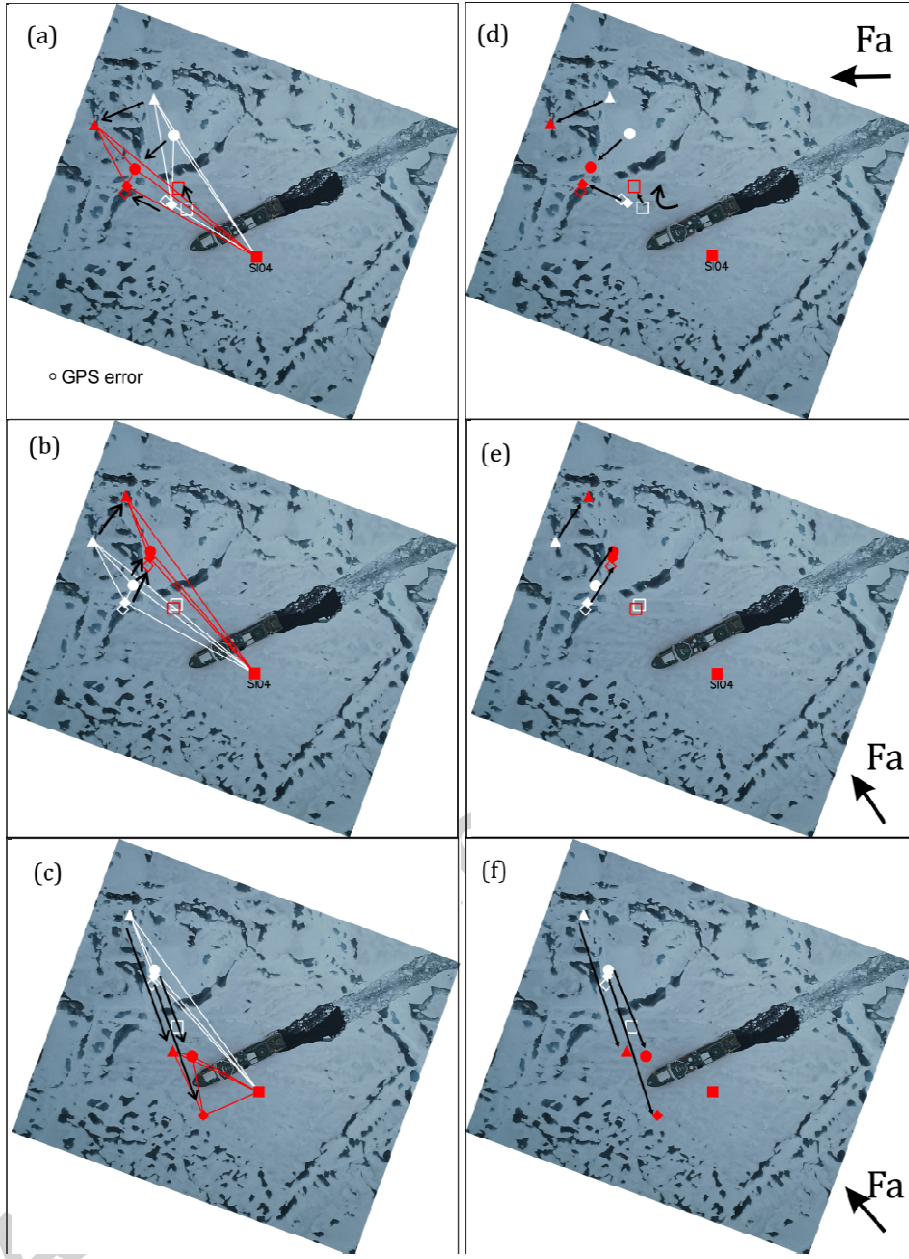


**Figure 6** Deformation of buoy arrays during the (a)&(d) D13, (b)&(e) D16, and (c)&(f) D21 events. In the left panels, the white and red lines represent the buoy arrays before and after the events, respectively. In all panels, black solid arrows show displacement relative to SI04. Closed square, circle, triangle, and diamond symbols mark the locations of SI04, KP03, KP04 and KP08, respectively, and open square and diamond symbols for that of SI03 and 2010I, respectively.  $F_a$  is the direction of wind stress. The aerial photography and buoy arrays of August 14 (Figure 1) here rotated for the floe orientation on December 13. Black circle in (a) is the IMB GPS error estimate (4 m), drawn to scale.

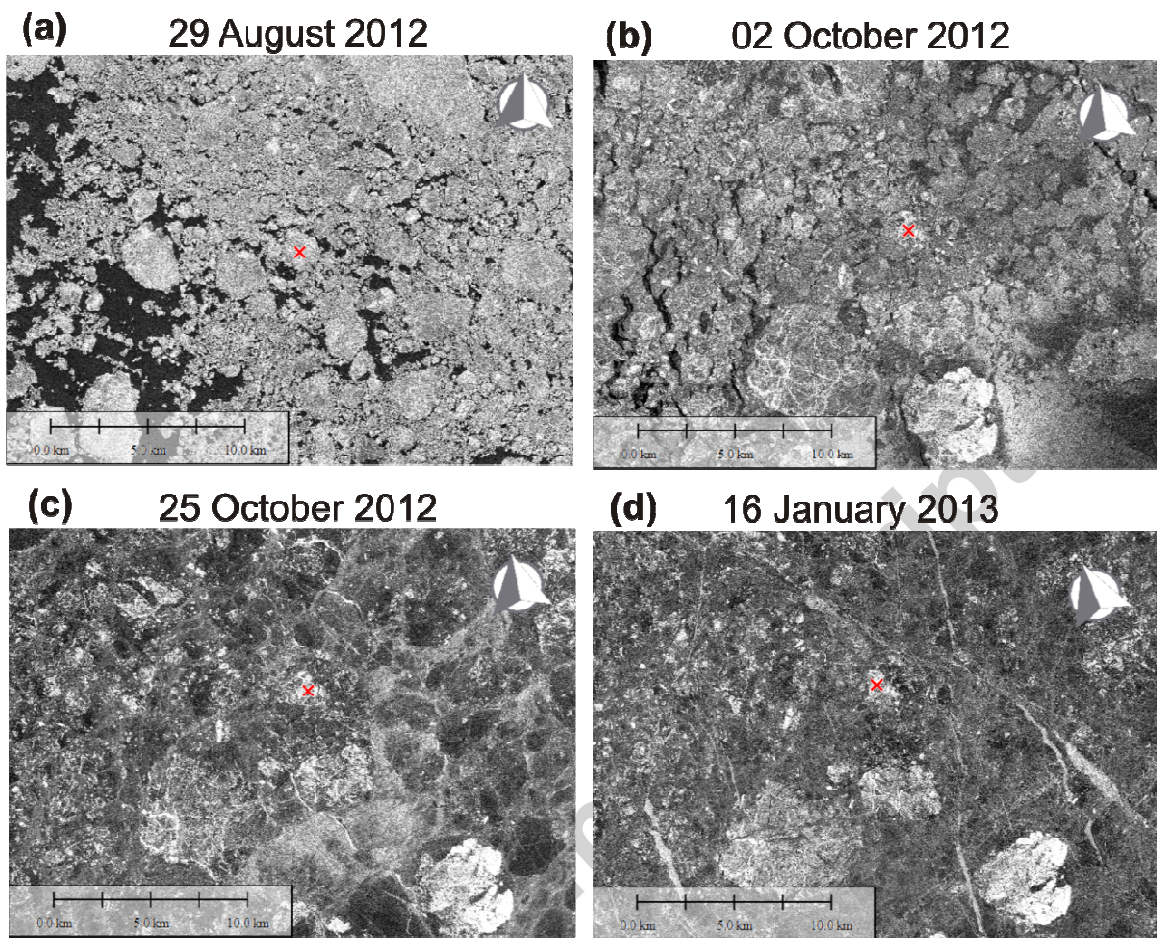


**Figure 7** TerraSAR-X ScanSAR image (©DLR) acquired on (a) 29 August 2012, (b) 2 October 2012, (c) 25 October 2012, and (d) 16 January 2013. The location of the ice floe is marked as red x in the middle of each image. The spatial scale of the image is shown on the bottom left and a compass on the top right corner of each image. Each image covers an area of 35 by 35 km. In the image, grey tone indicates the strength of backscattering, i.e., darker tone is low backscattering and brighter tone is high backscattering. For example, calm open water is shown in black dark tone, and multiyear ice floes in much brighter tone.

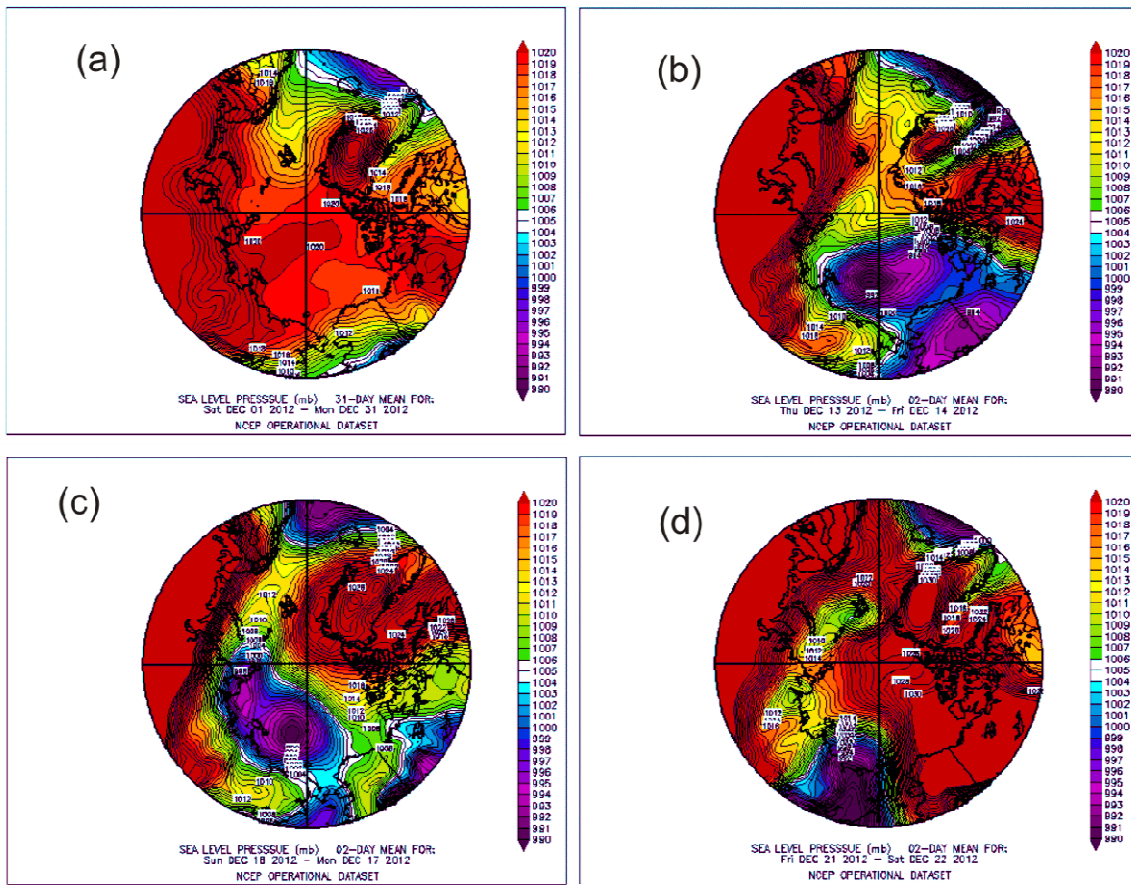


**Figure 8** Sea level pressure maps (a) during December 2012, (b) on December 13, (c) on December 17, and (d) on December 21. The plots were created from the NCEP Operational Plotting Page (<http://www.esrl.noaa.gov/psd/data/histdata/>).

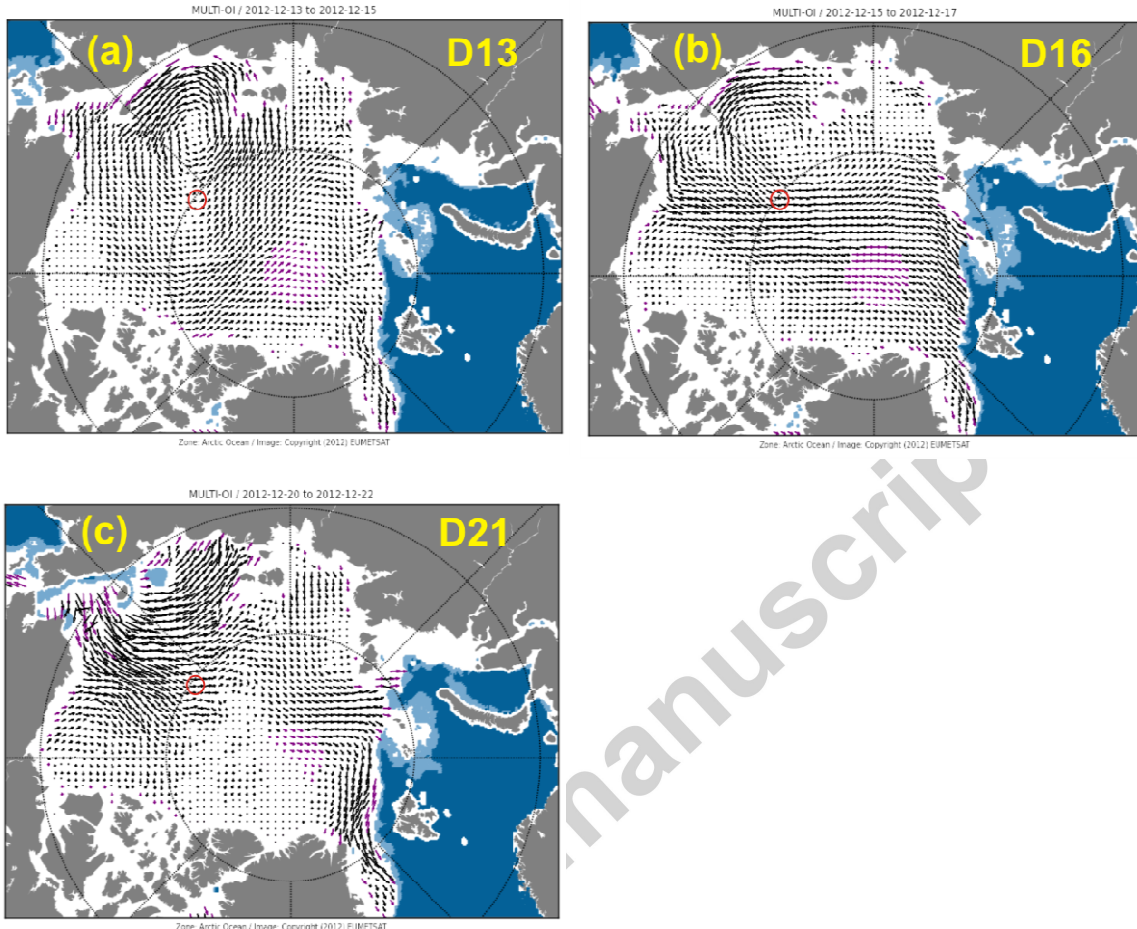


**Figure 9** Satellite ice drift maps during the three deformation events, (a) D13, (b) D16, and (c) D21. The images were downloaded from EUMETSAT's Ocean and Sea Ice (OSI) Satellite Application Facility (SAF) High Latitude (HL) Processing Centre (<http://osisaf.met.no/>).

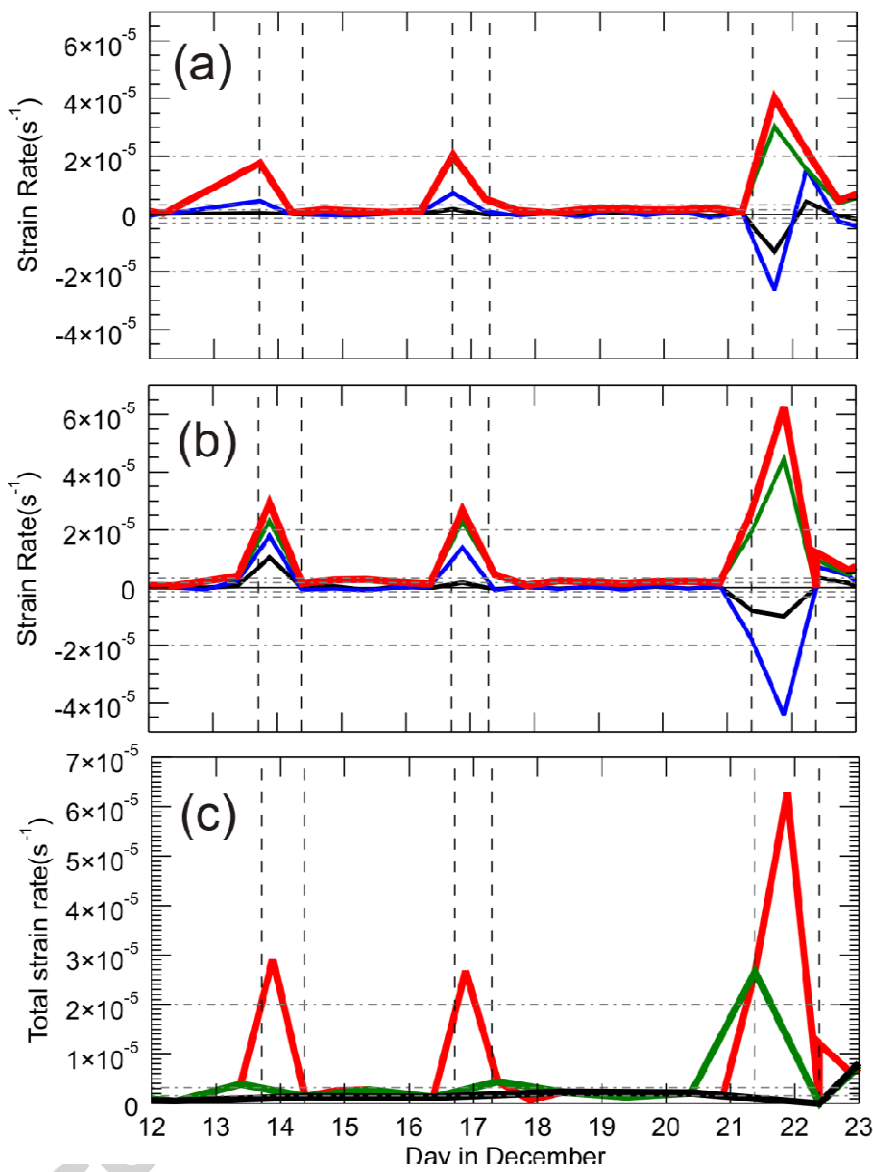


**Figure 10** Strain rates calculated from the pair of (a) SI04-KP03 and (b) SI04-KP08 for the 12-h time scale. In (a) and (b) solid black, blue, green, and red lines are strain rates estimated from baseline length ( $\varepsilon_L$ ), divergence ( $\varepsilon_d$ ), shear ( $\varepsilon_s$ ), and total deformation ( $\varepsilon_t$ ). In (c) total strain rates ( $\varepsilon_t$ ) of SI04-KP08 are shown for the time scale of 12 hours (red line), 1 day (green line), and 2 days (black line). In all plots three thin horizontal (grey) dash-dot lines are the error estimates for the strain rate for the time scale of 1 hour, 6 hours and 9 hours (see text). The error lines for the time scale of 1 hour are furthest from the zero, and the ones for the time scale of 9 hours are closest to zero.

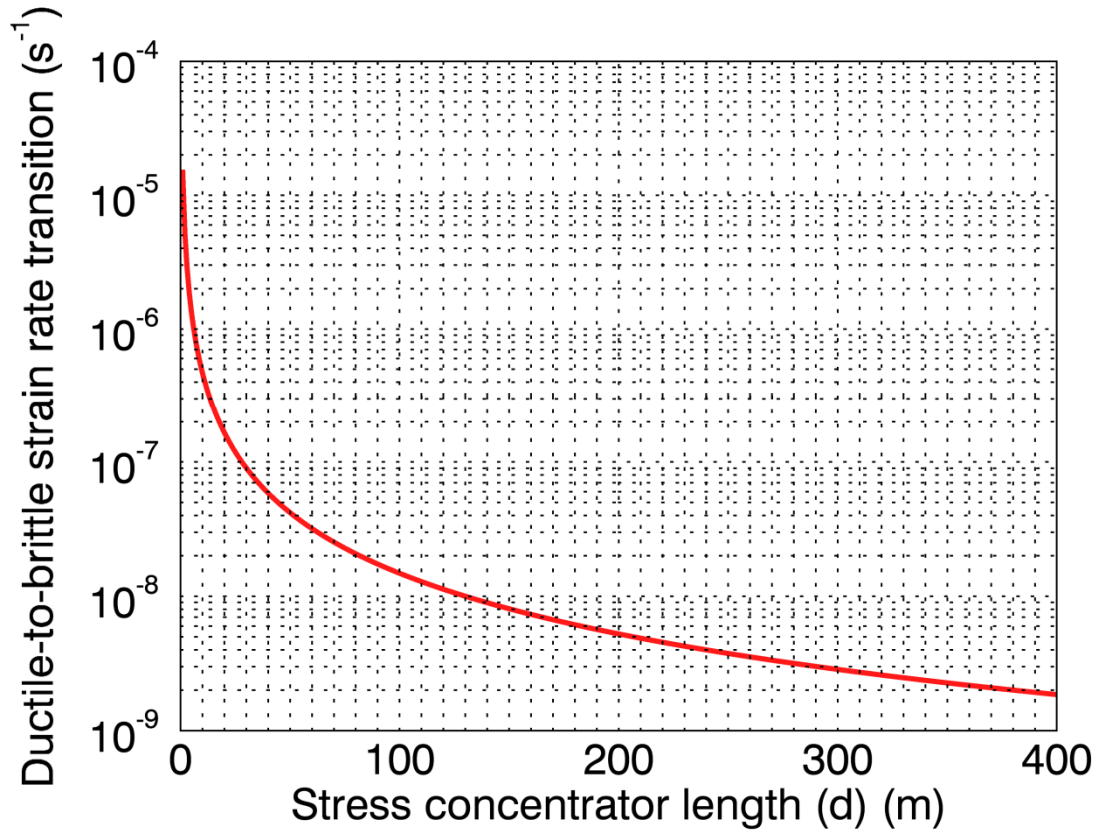


**Figure 11** Ductile-to-brittle strain rate transition as a function of the length of stress concentrators (crack/lead)  $d$ . The strain rate transition was calculated from Eq. 21 in Schulson (2001) using the same values for all model parameters but with  $d$  varying between 0 and 400 m.

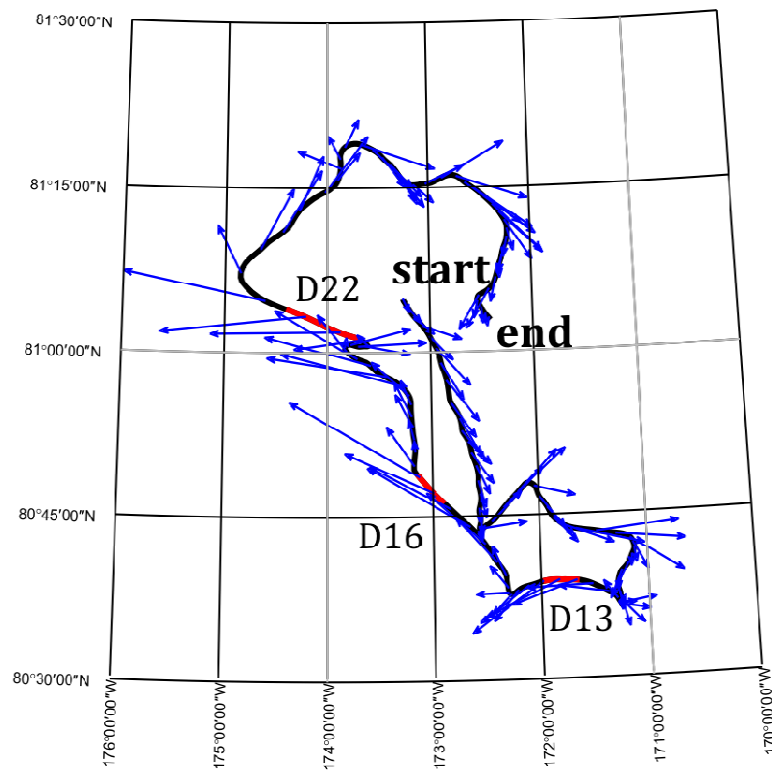


**Figure 12** Wind vectors along the drift track of the floe. The three deformation periods are highlighted in red in the drift track.

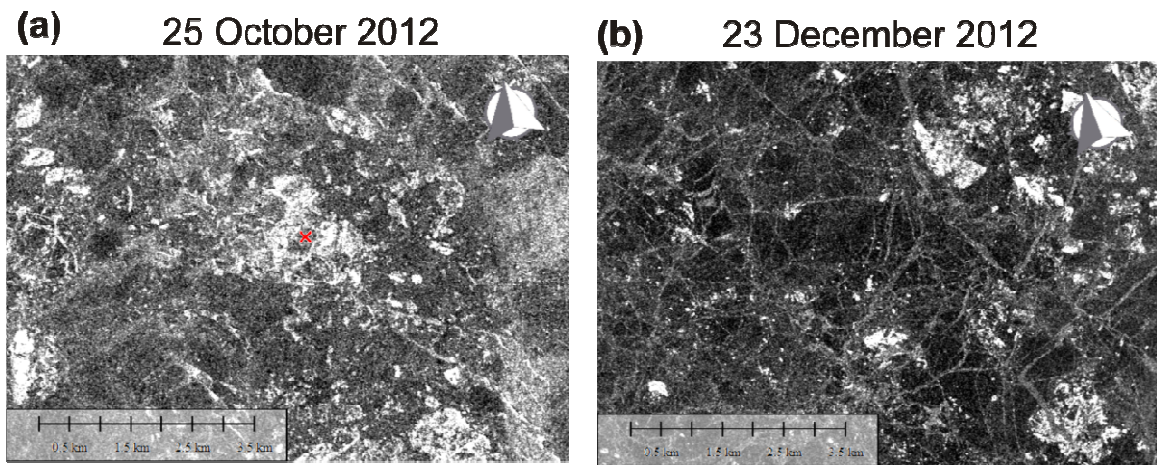


**Figure 13** TerraSAR-X ScanSAR image (©DLR) acquired on (a) 25 October 2012 and (b) 23 December 2012. The images cover the area of 7 km by 10 km, and red x mark in (a) indicates the location of SI04 at the time of image taken. The December 23 image shows the area about 30 km from the buoy location (no image available at the buoy location on that day). The spatial scale of the image is shown bottom left and compass in the top right corner of each image. In the image grey tone indicates the strength of backscattering, i.e., darker tone is low backscattering and brighter tone is high backscattering. In (b) darker grey tone indicates young growing ice and thin lines of brighter tone are the fracture lines. Multiyear ice floes are shown in much brighter tone.